Transient, synobduction exhumation of Zagros blueschists inferred from P-T, deformation, time, and kinematic constraints: Implications for Neotethyan wedge dynamics

P. Agard,[1] P. Monié,[2] W. Gerber,[1] J. Omrani,[1,3] M. Molinaro,[4] B. Meyer,[1] L. Labrousse,[1] B. Vrielynck,[1] L. Jolivet,[1] and P. Yamato[1]

Received 11 October 2005; revised 10 March 2006; accepted 5 June 2006; published 2 November 2006.

[1] We present the first P-T, deformation time, and kinematic constraints on the only known blueschist facies rocks (BS) present in the Zagros (Hajiabad area). The BS were underplated below the Sanandaj-Sirjan zone and crop out as kilometer-scale bodies within extensive colored melange units marking discontinuously the Neotethyan suture zone. P-T estimates point to high-pressure/low-temperature (HP-LT) conditions around 11 kbar and 520–530°C for the majority of BS, along a ~15°C km^{-1} gradient. Some exotic blocks in matrix serpentinite reached 17–18 kbar at ~500°C. In situ laser probe ^{40}Ar-^{39}Ar radiometric age constraints on phengite cluster between 85 and 95 Ma and suggest that (1) synconvergence exhumation of Zagros BS from 35–50 km to depths <15–20 km was accomplished before 80 Ma, (2) BS exhumation corresponded to a transient process with respect to the long-lived subduction beneath Iran (~150–35 Ma), and (3) age constraints for Zagros BS are 5–10 Myr older than for the nearby Oman HP-LT rocks and broadly coincide with obduction processes in the region (circa 95–70 Ma). We propose that the mechanical coupling across the Neotethyan subduction zone (NSZ) beneath Iran was modified by the large-scale plate rearrangement accompanying obduction, allowing for a short-lived exhumation of Zagros BS. Exhumation ceased at the end of obduction, when subduction of the Arabian continental margin stopped. Kinematic calculations suggest that convergence velocities across the NSZ likely doubled (to ~5–6 cm yr^{-1}) during the period 118–85 Ma, so that BS exhumation may have been promoted by a combination of obduction movements and increased convergence velocities.

Citation: Agard, P., P. Monié, W. Gerber, J. Omrani, M. Molinaro, B. Meyer, L. Labrousse, B. Vrielynck, L. Jolivet, and P. Yamato (2006), Transient, synobduction exhumation of Zagros blueschists inferred from P-T, deformation, time, and kinematic constraints: Implications for Neotethyan wedge dynamics, *J. Geophys. Res.*, *111*, B11401, doi:10.1029/2005JB004103.

1. Introduction

[2] The Zagros orogen (Figure 1a) has long remained poorly known within the Alpine collision zone and its geodynamic evolution is the target of recent research efforts [e.g., *Talebian and Jackson*, 2002; *Walker and Jackson*, 2002; *Hatzfeld et al.*, 2003; *Regard et al.*, 2003; *Allen et al.*, 2004; *Ghazi et al.*, 2004; *McQuarrie*, 2004; *Sepehr and Cosgrove*, 2004; *Vernant et al.*, 2004; *Agard et al.*, 2005a; *Meyer et al.*, 2005; *Molinaro et al.*, 2005; *Paul et al.*, 2006]. Surprisingly, unlike most classical subduction-collision Alpine belts, the Zagros almost completely lacks subduction relics such as blueschist facies metamorphic rocks [*Ernst*, 1972; *Okay*, 1989; *Maruyama et al.*, 1996]. Blueschists (BS) in fact represent one of the key petrological records of vertical displacements at plate boundaries leading to the global recycling of material in both mantle and arcs [e.g., *Ricard and Vigny*, 1989; *Bebout*, 1996], particularly in as much as they record the thermal regime of subduction zones [e.g., *Cloos*, 1985; *Peacock*, 1990; *Okay*, 2002; *Agard et al.*, 2005b]. They also bring insights into past geodynamic processes [e.g., *Ernst*, 1988] and help constrain regional-scale paleoreconstructions [e.g., *Sengör et al.*, 1988; *Dercourt et al.*, 1993, 2000; *Stampfli and Borel*, 2002; *Jolivet et al.*, 2003].

[3] Despite a relative consensus on their formation in subduction zones, the way blueschists, and HP-LT rocks in general, are brought back to the surface still is the matter of considerable debate. Models (for a review, see *Platt* [1993]) either emphasize the dynamics of accretionary wedges [*Cloos*, 1982; *Shreve and Cloos*, 1986], the role of buoyancy forces [*Chemenda et al.*, 1995; *Von Blanckenburg and Davies*, 1995], tectonic thinning [*Platt*, 1986; *Hubbard et*

[1] Laboratoire de Tectonique, UMR CNRS 7072, Université Paris 6, Paris, France.
[2] Laboratoire Dynamique de la Lithosphère, UMR CNRS 5573, Université Montpellier 2, Montpellier, France.
[3] Also at Geological Survey of Iran, Tehran, Iran.
[4] Laboratoire de Tectonique, Université de Cergy Pontoise, Cergy, France.

0148-0227/06/2005JB004103$09.00

al., 1995], mechanical decoupling (e.g., by the hydration of the fore arc [*Gerya et al.*, 2002]; through metamorphic reactions [*Jolivet et al.*, 2005]), tectonic underplating and erosion [*Ring and Brandon*, 1999], or a combination of these factors [e.g., *Platt*, 2000; *Burov et al.*, 2001; *Jolivet et al.*, 2003].

[4] We present below the results of a study devoted to the exhumation of the only blueschists reported so far along the ~3000 km long Zagros orogen [*Sabzehei*, 1974], despite an enduring subduction history (circa 150–35 Ma [e.g., *Berberian and King*, 1981; *Sengör et al.*, 1988; *McCall*, 1997]). Hajiabad-Esfandageh blueschists (Hajiabad BS, in the following) crop out in the southeasternmost Zagros amongst other units of partly oceanic affinity (the so-called colored melange [*Gansser*, 1955]), but their precise tectonic setting, at the rear of the Main Zagros Thrust (MZT), is still obscure [*Sabzehei et al.*, 1994] (Figure 1b). The Neotethyan suture zone is generally assumed to lie along the MZT by the majority of workers, but its location has been put into doubt by some [e.g., *Alavi*, 1994]. In this sense, the general lack of BS in the Zagros clearly adds to the uncertainty on this issue.

[5] One of the aims of this paper is to bring first-order constraints on the tectonic setting, nature, age and genetic conditions of these blueschists. The petrology of the Hajiabad BS was only investigated by *Sabzehei* [1974], who favored a metasomatic origin, at a time when the relationship between BS belts and convergent margins had only recently been established [*Ernst*, 1972]. Electron probe microanalyses and P-T estimates are completely lacking. This HP-LT metamorphism was thought to have taken place during the Oligocene [*Sabzehei*, 1974], but the four K/Ar ages published so far, at 79.0 ± 1.5 and 82.4 ± 1.4 Ma [*Ghasemi et al.*, 2002], 98.6 ± 2.4 and 101.2 ± 2.4 Ma [*Delaloye and Desmons*, 1980] likely suggest a Cretaceous age. Why the only blueschists in the Zagros crop out close to the Makran (where subduction is still active; [*Platt et al.*, 1985; *Regard et al.*, 2003]) and what is their relationship with the nearby Oman blueschists [e.g., *Goffé et al.*, 1988; *Searle et al.*, 2004] are key issues.

[6] We discuss the tectonic setting of these BS and provide pressure-temperature-deformation-time (P-T-ε-t) constraints on their evolution using metamorphic petrology and in situ laser ablation ^{40}Ar-^{39}Ar dating on phengite. We will show that a transient exhumation process brought back these BS from subduction depths >35–40 km to midcrustal depths of <15–20 km by 80 Ma. We then provide kinematic estimates of convergence velocities during the period 145–65 Ma in order to better constrain the geodynamic context of BS formation and exhumation. Implications in terms of regional geodynamics and wedge dynamics are finally discussed.

2. Tectonic Setting of Blueschist Facies Occurrences

2.1. Regional Setting: Where Do the Blueschists Belong?

[7] The Zagros orogen is a young Tertiary collision belt [*Schröder*, 1944; *Stöcklin*, 1968; *Berberian and King*, 1981; *Jackson et al.*, 1995; *Hessami et al.*, 2001; *Allen et al.*, 2004] generally considered a recent analogue of the Himalayan orogen. Collision developed following a long-lasting NE vergent subduction of the Neotethyan ocean and of part of the Arabian passive margin beneath Eurasia [e.g., *Ricou*, 1994; *Dercourt et al.*, 1993, 2000]. Subduction was accompanied by a widespread Mesozoic and syn- to post-Eocene calk-alkaline magmatism in the upper plate, along the Sanandaj-Sirjan zone (SSZ) and the Urumieh-Dokhtar magmatic arc (UDMA), respectively (Figure 1a). The SSZ [*Stöcklin*, 1968; *Braud*, 1987], which forms the continental collage of Iran together with the Lut block and central Iran [e.g., *Ricou*, 1994], extends from the Bitlis area in Turkey to the western end of Makran [*Sengör et al.*, 1988; *McCall and Kidd*, 1981], across the present-day transition zone from collision (Zagros) to subduction (Makran; Figure 1b). In the NW Zagros, *Agard et al.* [2005a] showed that the subduction beneath the Iran continental collage had ceased by circa 35 Ma and that collision had started before 25–23 Ma.

[8] Metamorphics mapped as blueschist facies rocks are shown in the Hajiabad 1:250,000-scale map [*Sabzehei et al.*, 1994] in five main areas investigated in the present study (Figures 1b and 2). Hajiabad BS are found in the upper plate of the present-day collisional setting, at the rear of the Main Zagros Thrust (MZT). Similarly, the few BS outcrops from Makran reported so far (Fannuj BS, Figure 1b [*McCall*, 1997]) are also located in the upper plate far north of today's oceanic accretionary wedge [*Platt et al.*, 1985] and dated at 87.9 ± 5.5 Ma [*Delaloye and Desmons*, 1980]. In contrast, the circa 85–80 Ma Oman BS and eclogites are exposed below the obducted Semail ophiolite (Figure 1a) [*Searle et al.*, 2004], whose Zagros equivalent is the Neyriz ophiolite underlying the MZT (Figure 1b) [*Ricou*, 1971; *Lanphere and Pamic*, 1983]. No equivalent HP-LT rocks have been found, however, below the Neyriz ophiolite.

[9] The Hajiabad BS are considered to lie within the colored melange south of the SSZ by some authors

Figure 1. (a) Structural sketch map of Iran and adjacent areas. Major thrust zones and faults are indicated. Dark blue and yellow patches are Eocene (UDMA, Urumieh-Dokhtar magmatic arc) and Mesozoic calc-alkaline magmatism (SSZ, Sanandaj-Sirjan zone), respectively. Black stars denote the occurrence of blueschist facies rocks. MZT, Main Zagros thrust. Thick black arrows denote present-day, NUVEL-1A plate motion relative to Eurasia [*DeMets et al.*, 1990]. The location of Figure 1b and inset (frames) is indicated. Inset shows the topography and the location of subcrustal events (red and white dots) with respect to superficial events (yellow dots). (b) Simplified structural map at the transition between collision (SE Zagros) and subduction (west Makran) showing the location of the SE Zagros colored melange (blue) and of major ophiolites (green). Obducted ophiolites are shown in brown. Black stars denote blueschist facies occurrences. Frame indicates location of Figure 2. The profiles of sections 2d and 2e are indicated. BD, Bajgan-Durkan complex; BS, blueschists; BZZG, Band e Zeyarat/Zemeshk/Ganj ophiolites; M*, transect studied by *Molinaro et al.* [2005]; MZT, Main Zagros thrust.

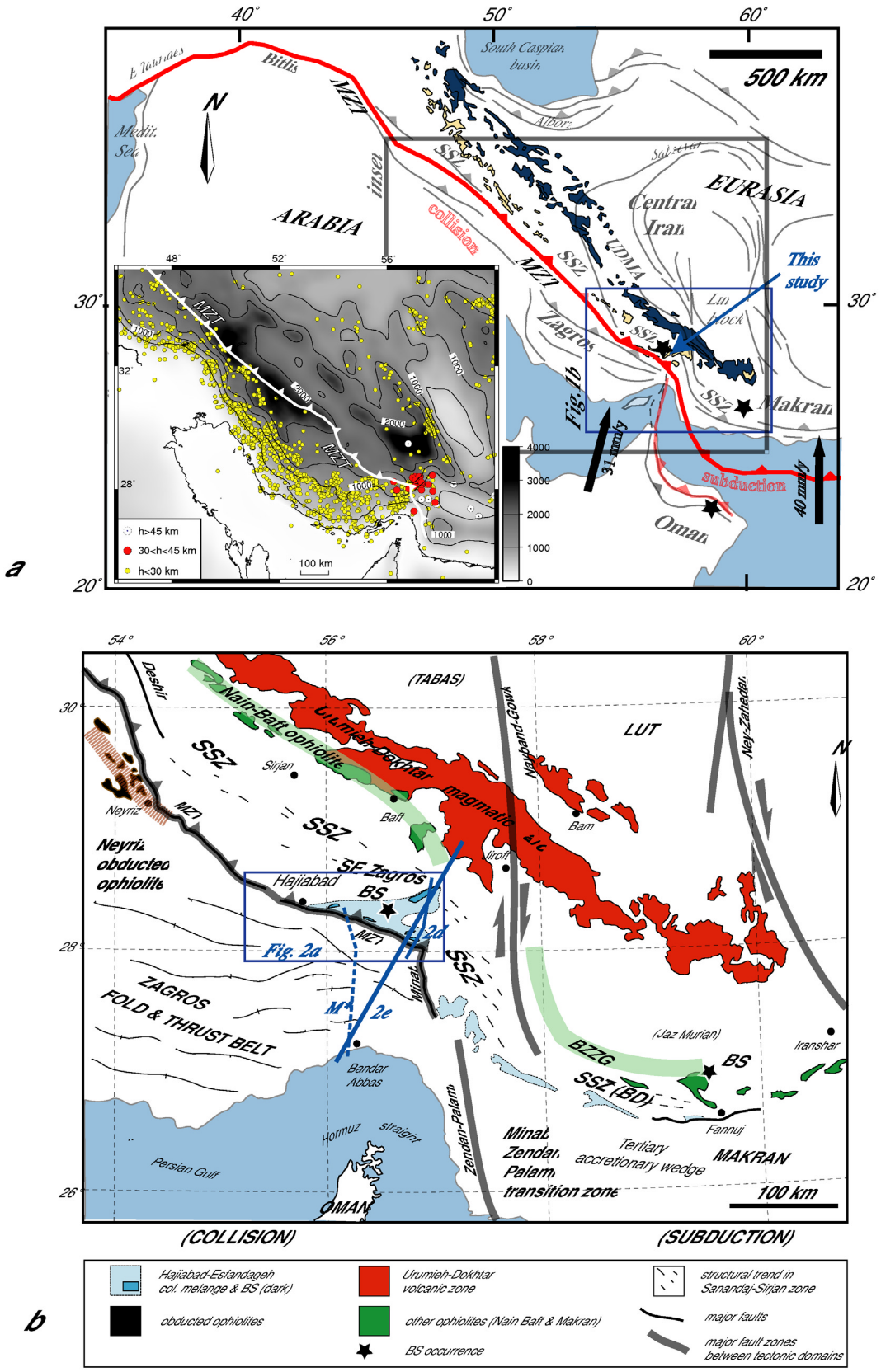
a
40°
50°
60°
30°
20°
500 km
N
South Caspian basin
Bitlis
MZT
ARABIA
EURASIA
Central Iran
collision
SSZ
UDMA
This study
Lut block
Zagros
Fig. 1b
31 mm/y
40 mm/y
subduction
Oman
Makran
Albors
48°
52°
56°
32°
28°
h>45 km
30<h<45 km
h<30 km
100 km
4000
3000
2000
1000
0
b
54°
56°
58°
60°
30
28
26
(TABAS)
Nain-Baft ophiolite
Urumieh-Dokhtar magmatic arc
LUT
Nayband-Gowk
Neyr-Zahedan
Sirjan
Baft
Bam
Jiroft
Neyriz
Neyriz obducted ophiolite
SF Zagros BS
Hajiabad
Fig. 2a
Fig. 2d
Fig. 2e
ZAGROS FOLD & THRUST BELT
Minab
Bandar Abbas
Hormuz straight
Persian Gulf
OMAN
Zendan-Palami
Minab Zendan Palami transition zone
(Jaz Murian)
BZZG
SSZ (BD)
BS
Iranshar
Fannuj
Tertiary accretionary wedge
MAKRAN
100 km
(COLLISION)
(SUBDUCTION)
Hajiabad-Esfandageh col. melange & BS (dark)
obducted ophiolites
Urumieh-Dokhtar volcanic zone
other ophiolites (Nain Baft & Makran)
BS occurrence
structural trend in Sanandaj-Sirjan zone
major faults
major fault zones between tectonic domains

Figure 1

[*Delaloye and Desmons*, 1980; *McCall*, 1997] but are imbricated both with the colored melange zone and the SSZ in the Hajiabad geological map [*Sabzehei et al.*, 1994] (Figures 2a and 2b). This "colored melange" [*Gansser*, 1955] contains abundant ultramafics (typically with antigorite) with chromite deposits, few gabbros and diabases, partly preserved volcano-sedimentary sequences with alkaline pillow lavas, *Globotruncana*-bearing red marls and radiolarites, and "exotic" marbles, amphibolites and minor blueschists. To the north of the SSZ, another colored melange crops out in the Upper Cretaceous–Paleocene Nain-Baft oceanic domain (NBD, Figure 1b) [*Davoudzadeh*, 1972; *McCall*, 1997], once a short-lived back-arc basin [*Arvin and Robinson*, 1994]. Despite a structural bend of both the Hajiabad BS and the Nain-Baft domain (Figure 1b), which tends to connect the two, the NBD vanishes to the SE and is not metamorphosed. We will show that the Hajiabad BS and its associated colored melange are not klippen from the NBD resting on top of the SSZ units, which refutes *Alavi*'s [1994] model.

2.2. Reappraisal of the Structural Map and Cross Sections

[10] On the basis of new investigations and on the Hajiabad 1:250,000-scale geological map [*Sabzehei et al.*, 1994] (Figure 2a), a reappraised structural map is proposed for the area (Figures 2b and 2c). An approximately N-S cross section was constructed east of the study area (Figure 2d). This cross section was included in a synthetic section across the whole Zagros orogen (Figure 2e), from the external fold-and-thrust belt [*Molinaro et al.*, 2005] to the UDMA.

[11] Figures 3a and 3b emphasizes the intensity of folding and the imbrication of BS facies and serpentinite units in the Ashin area. Blueschists are invariably juxtaposed with units from the colored melange. No direct contact between BS exposures and the SSZ was observed, so that BS represent lenses within the colored melange. Blueschist facies lithologies, which comprise alternating marbles and metavolcanics (Figure 3d), are closely associated, at all scales, with serpentinites. Units of the SSZ, particularly the Devonian basement, are resting as isolated klippen everywhere on top of the colored melange (Figure 3e). Rather than slices imbricated with the SSZ (Figure 2b), the BS crop out in the core of two large (~20 km; Figure 2c) anticline structures, continuous along strike, representing tectonic windows below the SSZ (Figure 2c).

[12] The BS and the matrix colored melange are thrust onto the Eo-Oligocene flysch domain. The SSZ is also thrust onto the flysch domain (e.g., Paleozoic SSZ klippen on Figure 2a). This latter thrust was cut by the former contact, and the order of thrust emplacement is indicated on the cross section of Figure 2d. The whole of the internal zones was finally uplifted and domed, allowing for the erosion of the SSZ and for the BS exposure.

[13] The cross section of Figure 2d points to the existence of variably, locally metamorphosed units in the colored melange and to the existence of large-scale folds outlined by pelagic Cretaceous limestones (Figure 3f). Original oceanic sequences, with serpentinites underlying gabbros and pillow lavas are still preserved in places (Figures 2d and 3g) but show only incipient BS facies metamorphism (e.g., west of Seghina, Figure 2a). Most BS facies units, with the exception of the "serpentinite glaucophane" Seghina unit (see section 3.1), are strongly refolded hectometric to kilometric slices wrapped in a serpentinite-rich matrix. They do not, therefore, represent isolated, exotic boulders such as the knockers of the Franciscan melange [e.g., *Platt*, 1993, and references therein]. This pattern also contrasts with those of colored melange areas in the strictest sense, where a mixture of limestone slivers, minor lavas, radiolarites and serpentinites crop out in a disorganized fashion (Figure 3h) with much less folding and flattening (see below).

2.3. Deformation Patterns

[14] Stretching lineations, together with sampling sites, are shown in Figure 4. At the metric to hectometric scale, numerous folds are present in the blueschists (Figures 2d, 5a, and 5b) and flattening and recumbent folding largely dominate over shear movements. Schistosities vary significantly but tend to have an E-W direction (Figures 3a and 3b). Stretching lineations correspond for the most part to synexhumation upper greenschist to epidote amphibolite stages rather than to blueschist stages. BS facies lineations tend to be aligned along an E-W direction (Figures 5c and 5d), but are too rare for this observation to be statistically ascertained (Figures 4a–4d). This pattern could also be due to later flattening and boudinage. Late blueschist amphiboles can also, locally, be completely disoriented.

Figure 2. (a) Geological map of the study area after *Sabzehei et al.* [1994]. Blueschist bodies (blue) are found in five main areas (from west to SE, Hajiabad, Shadab, Seghina, Ashin and Sheikh Ali) in the colored melange (green). Frames: location of Figure 4a–4d. The profile of section in Figure 2d is indicated. The ^{40}Ar-^{39}Ar ages obtained in this study are indicated (see Figure 9b). The SSZ is composed of a predominantly Ordovician to Devonian basement, a Mesozoic cover including Jurassic calc-alkaline lavas, Lower Cretaceous alternating lavas and limestones and the characteristic Mid to Upper Cretaceous Orbitolina limestone [*Stöcklin*, 1968]. It also comprises mafic to ultramafic bodies (e.g., Sikhoran complex, south of Ashin) emplaced during the Late Carboniferous and rejuvenated during Late Permian to Triassic times [*Ghasemi et al.*, 2002]. (b) Structural sketch map after *Sabzehei et al.* [1994]. (c) Reappraisal of the structural sketch map (this study). The colored melange is interpreted as a window below the SSZ, exposed by a late antiformal doming of the nappe pile. (d) Approximately N-S section constructed across Sheikh Ali and Ashin (location on Figure 2a). Numbers 1 to 4 refer to the sequence of thrust emplacement. The location of Figure 3 photographs is indicated. The existence of the deep thrust featured below the colored melange is supported by the deep seismic activity shown on Figure 1a. BS, blueschist; GS, greenschist; MZT, Main Zagros thrust; ZFTB, Zagros fold and thrust belt. (e) Approximately N-S section from the Persian Gulf to the UDMA (location on Figure 1b), from *Molinaro et al.* [2005] for the ZFTB and this study for the internal zones. HZF, High Zagros fault; MFF, Main front fault; Tr-J, Triassic to Jurassic cover.

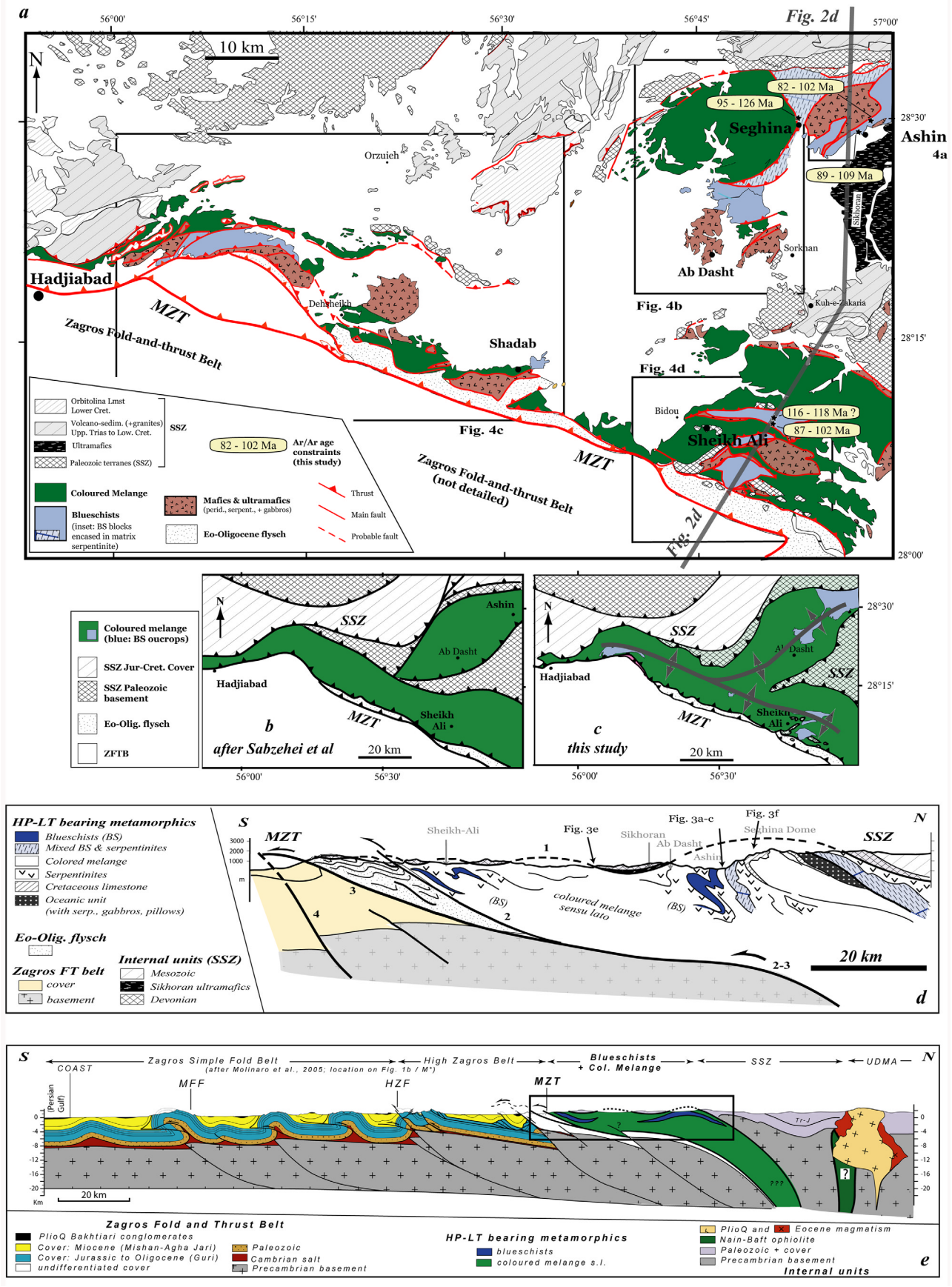
a
Fig. 2d
10 km
N
Orzuieh
Seghina
82 - 102 Ma
95 - 126 Ma
89 - 109 Ma
Ashin
4a
Sikhoran
Sorkhan
Ab Dasht
Hadjiabad
MZT
Zagros Fold-and-thrust Belt
Dehsheikh
Shadab
Fig. 4b
Fig. 4d
Fig. 4c
Kuh-e-Zakaria
Bidou
116 - 118 Ma ?
87 - 102 Ma
Sheikh Ali
Zagros Fold-and-thrust Belt (not detailed)
Fig. 2d
Orbitolina Lmst Lower Cret.
Volcano-sedim. (+granites) Upp. Trias to Low. Cret.
Ultramafics
Paleozoic terranes (SSZ)
SSZ
Ar/Ar age constraints (this study)
Coloured Melange
Blueschists (inset: BS blocks encased in matrix serpentinite)
Mafics & ultramafics (perid., serpent., + gabbros)
Eo-Oligocene flysch
Thrust
Main fault
Probable fault
56°00'
56°15'
56°30'
56°45'
57°00'
28°30'
28°15'
28°00'
Coloured melange (blue: BS oucrops)
SSZ Jur-Cret. Cover
SSZ Paleozoic basement
Eo-Olig. flysch
ZFTB
b
after Sabzehei et al
20 km
c
this study
HP-LT bearing metamorphics
Blueschists (BS)
Mixed BS & serpentinites
Colored melange
Serpentinites
Cretaceous limestone
Oceanic unit (with serp., gabbros, pillows)
Eo-Olig. flysch
Zagros FT belt
cover
basement
Internal units (SSZ)
Mesozoic
Sikhoran ultramafics
Devonian
S
N
Sheikh-Ali
Fig. 3e
Fig. 3a-c
Fig. 3f
Sikhoran
Ab Dasht
Ashin
Seghina Dome
3000
2000
1000
m
1
2
3
4
(BS)
coloured melange sensu lato
2-3
20 km
d
COAST
Zagros Simple Fold Belt
(after Molinaro et al., 2005; location on Fig. 1b / M*)
High Zagros Belt
Blueschists + Col. Melange
SSZ
UDMA
MFF
HZF
MZT
(Persian Gulf)
Km
20 km
Zagros Fold and Thrust Belt
PlioQ Bakhtiari conglomerates
Cover: Miocene (Mishan-Agha Jari)
Cover: Jurassic to Oligocene (Guri)
undifferentiated cover
Paleozoic
Cambrian salt
Precambrian basement
HP-LT bearing metamorphics
blueschists
coloured melange s.l.
PlioQ and Eocene magmatism
Nain-Baft ophiolite
Paleozoic + cover
Precambrian basement
Internal units
e

Figure 2

[15] Lineation maps show that GS stretching was dominantly E-W, except in the Sheikh Ali area, located close to the MZT (Figure 4d), and north of Ashin area (Figure 4a). Deformation is relatively coaxial (Figures 5e and 5f), with few spectacular kinematic indicators, and a dominant sense of shear can rarely be inferred. Stretching is also marked by a meter-scale E-W boudinage of epidote blueschists (Figure 5g). Given the predominance of folding and the relative coaxiality of the deformation, we propose that these lineations correspond to a component of E-W boudinage accompanying folding and flattening during exhumation, as reported from a number of other tectonic settings [e.g., *Labrousse et al.*, 2004, and references therein].

[16] From these observations, the most prominent features are as follows:

[17] 1. The blueschists are exposed as hectometric to kilometric bodies (or lenses) in the colored melange zone, the latter forming a tectonic domain of its own between the SSZ and the Eo-Oligocene flysch.

[18] 2. Deformation patterns and the thrust sequence suggest that these BS equilibrated at depths were underplated below the SSZ relatively early in the tectonic history. They were later exposed as a result of the general doming of the area.

[19] 3. Deformation patterns are dominated by flattening and boudinage rather than shear movements. E-W lineations, which are relatively scattered, are associated with greenschist facies exhumation.

3. Sample Description and Mineralogy

[20] Sampling sites are given in Figure 4 and in Table 1 (for other see Table S1 in the auxiliary material).[1]

3.1. Lithologies and Parageneses

[21] The protolith lithologies mainly correspond to metatuffs or marbles alternating with metavolcanics (dominantly metabasalts). The metatuffs locally comprise a large silty/sandy component, and resemble quartz-rich metagraywackes. No metapelites were found. In general, there is a systematic association between blueschist facies rocks and serpentinites wrapping the BS. A distinction should be made, however, between outcrops with hectometer- to kilometer-sized coherent tracts of BS (Ashin, Sheikh Ali; Figures 4a and 4d) and outcrops with meter to decimeter sized BS knockers wrapped in a serpentinite-rich matrix. (Seghina area; Figures 2a and 4b). The latter BS-bearing units were mapped as serpentinite glaucophane schists [*Sabzehei et al.*, 1994].

[22] The age of the protolith is unknown but thought pre-Cretaceous [*Sabzehei*, 1974]. The metamorphosed alternations strongly resemble the Lower Cretaceous arc series made of limestones and basalt flows, which crop out in the nearby SSZ or in northern Zagros [*Braud*, 1987; *Agard et al.*, 2005a]. The mafic to intermediate composition of the protoliths is reflected by the main parageneses, which comprise Gt-Phg-Chl-Rt±Ep±Amph±Ti±Bt (e.g., samples 3.01b, 3.12d, 3.28a; abbreviations after *Kretz* [1983]), Amph-Ep-Phg-Chl-Rt±Ab±Gt±Ti (e.g., samples 4.28a, 4.35c) or Amph-Lws-Cpx-Phg-Rt (sample 4.20a). Impure marbles contain large, millimeter- to centimeter-sized phengite, oxides and infrequent tiny blue amphiboles. The blueschists are typically overprinted by an upper greenschist to epidote amphibolite facies metamorphism of variable intensity (Figure 5h).

[23] Our samples, because they were mainly taken from meter-sized boudins preserved from retrogression, show little key syntectonic textural features but the following deformation-crystallization relationships can be outlined:

[24] 1. In several samples, garnet appears in textural equilibrium with blue amphibole, epidote, phengite and chlorite (Figures 6a and 6b). Garnet is replaced by chlorite and phengite in intermediate grade rocks and displays irregular rims (Figure 6c).

[25] 2. In some samples, blue amphibole replaces greenish blue amphibole (Figure 6d), in apparent equilibrium with garnet (Figure 6e). Relics of biotite and greenish blue amphibole are present in the matrix of sample 4.37b and biotite inclusions together with greenish blue amphibole are found in garnet cores from sample 3.12d (Figure 6e).

[26] 3. The typical blue amphibole-epidote-phengite-chlorite assemblage occurs as synkinematic pressure shadows around albite porphyroblasts (Figure 6f). Similarly, synkinematic chlorite-phengite pairs occurring along millimeter-sized shear bands (e.g., 3.27a, Figure 6g; see below) were used with TWEEQU [*Berman*, 1991] (see below).

[27] 4. Clinopyroxene, which appears as small crystals ($\sim$100 μm; Figure 6h) replacing probable magmatic clinopyroxene pseudomorphs in sample 4.20a, is in apparent equilibrium with lawsonite, glaucophane and phengite. Titanite is in equilibrium with or replaces rutile.

[28] In Gt-Phg-Chl-Rt±Ep±Amph±Ti±Bt assemblages, we can therefore identify three parageneses corresponding to successive reequilibration steps: P1, greenish blue amphibole + garnet cores ± Bt; P2, blue amphibole + garnet rims + phengite + epidote + Rt ± Chl; and P3, chlorite and phengite ± Ab.

3.2. Mineral Chemistry

[29] Mineral analysis was performed with Camebax SX50 and SX100 electron microprobes at University Paris VI (15kV, 10nA, WDS) using Fe2O3 (Fe), MnTiO3 (Mn, Ti), diopside (Mg, Si), CaF2 (F), orthoclase (Al, K), anorthite (Ca) and albite (Na) as standards.

3.2.1. Blue Amphiboles

[30] Dominantly blue amphiboles are found in areas preserved from retrograde metamorphism or in boudins (e.g., Figure 5g). Elsewhere actinolite and hornblende occur in late pods near major contacts with the serpentinites bodies, but these two types were not further studied. Amphibole compositions vary largely in the metamorphosed BS facies rocks. According to the classification of *Leake et al.* [1997], amphiboles range between barroisite and glaucophane (Figure 7a), with a clear chronological trend toward glaucophane (Figure 7b). Sodic amphiboles cluster in two groups, one between crossite and glaucophane s.s., one around riebeckite. For the former group, a clear evolution from crossite to glaucophane compositions is also evident (Figure 7c).

3.2.2. Phengite

[31] White mica compositions are mostly phengitic with variations along the tschermak Si(Fe,Mg) = AlAl exchange

[1] Auxiliary materials are available at ftp://ftp.agu.org/apend/jb/2005jb004103.

vector between muscovite and celadonite, as shown by Figure 7d. Si content is higher in metabasites (4.28a, 4.35c), particularly the exceptionally high content of sample 4.20a (Si = 3.7). On the other hand, departure from the purely phengitic substitution line is observed for almost all samples (Figure 7d), which suggests that a certain amount of ferric iron is present.

3.2.3. Chlorite

[32] Chlorite compositions mainly plot between clinochlore and daphnite (i.e., along the tschermak exchange

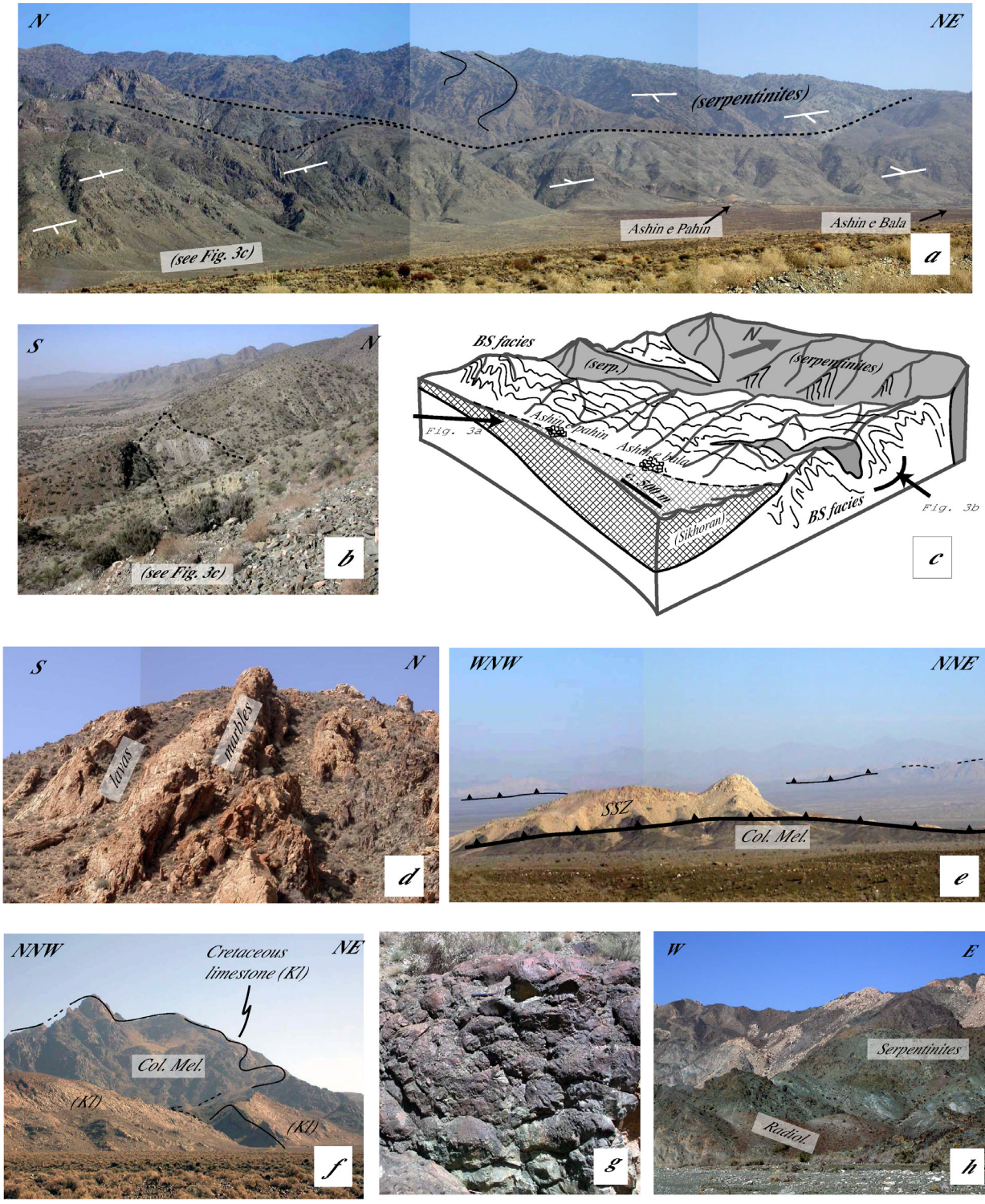

Figure 3

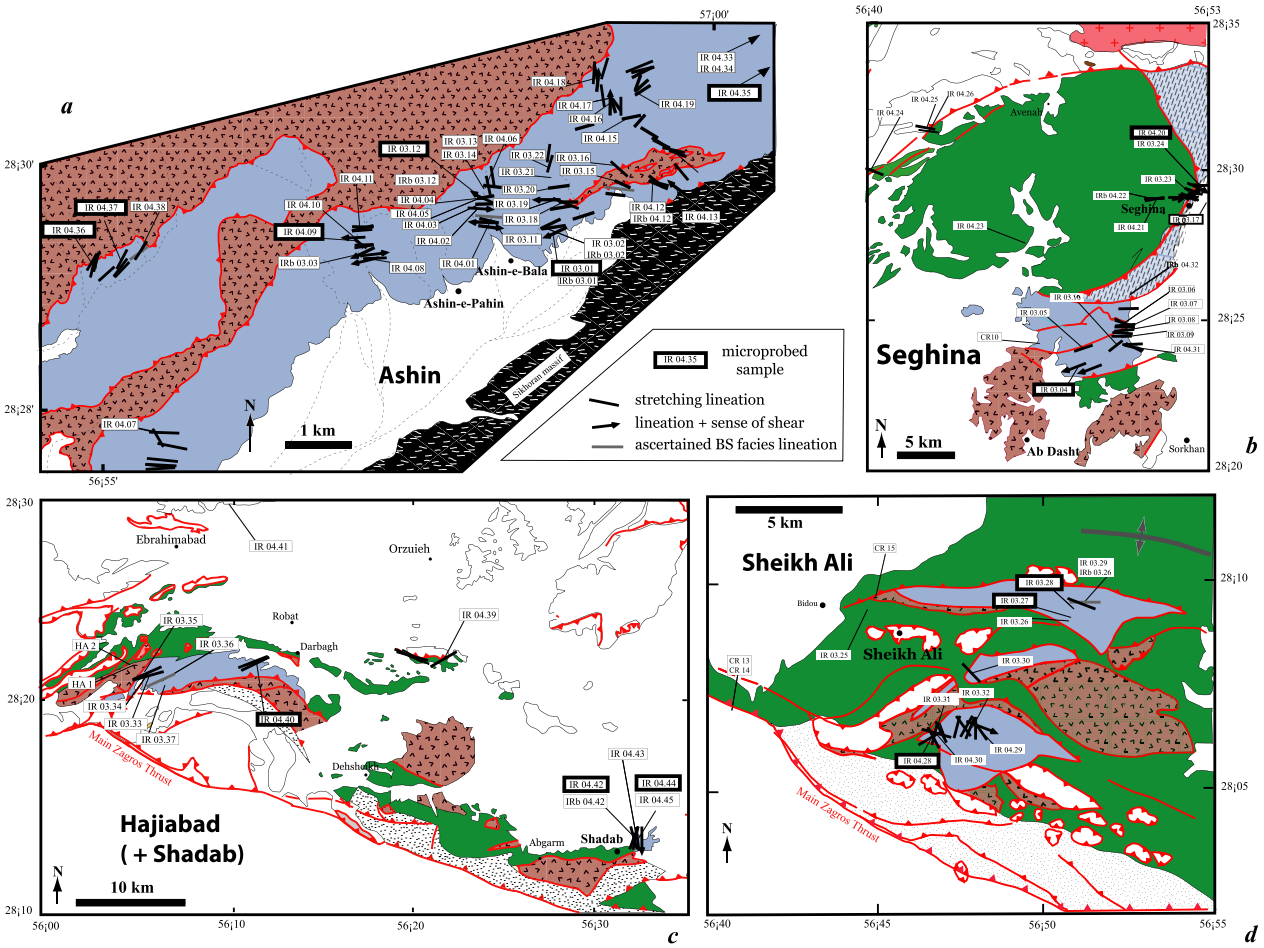

Figure 4. Close-up views of the four areas of Figure 2a showing sampling localities and measured lineations. Samples with a thick frame were studied with the electron probe microanalysis (Table 1; for others, see the auxiliary material). Light gray indicates blueschists. Dark gray indicates colored melange. Symbols are the same as for Figure 2a.

vector). Some samples from Sheikh Ali (3.27a, 3.28a) show a significant deviation toward sudoite (Figure 7e).

3.2.4. Garnet

[33] Garnets are dominantly ferrous, with X_{Mg} values ranging between 0.05 and 0.15 and slightly more magnesian cores (Figure 7f). The first-order evolution of garnet zonation is simple with a Ca and Mn decrease and a Fe and Mg increase toward the rim (Figure 7f). Profiles suggest only limited reequilibration on the garnet rims. Some garnets show a clear Mn enrichment in the cores which reflects low-grade growth zoning [*Spear and Selverstone*, 1983; *Spear*, 1993]. In detail, different patterns are encountered for intermediate composition rocks (e.g., 3.01b; 3.27a) and for metabasites (e.g., 3.12d). Oscillatory patterns were found only in the former type (Figure 7f).

3.2.5. Others

[34] Epidote compositions lie between zoisite and pistacite, with a pistacite component ranging between 40 and 80% but constant in each sample. Clinopyroxene was found only in sample 4.20a, with a composition intermediate between the jadeite and acmite end-members (and ~10% diopside), thus very close to or just within omphacitic

Figure 3. (a) Panoramic view to the NNE of Ashin outcrops highlighting the attitude of the foliation. (b) Serpentinite boudin (dashed contour) within the BS. (c) Three-dimensional diagram showing the attitude of the E-W trending foliation around Ashin and the imbrication of serpentinites and BS facies bodies at the hectometer scale. Views from the SW (Figure 3a) and from the east (Figure 3b) are located. (d) Steeply dipping, alternating lavas and marbles typifying Ashin BS lithologies. These series resemble Lower Cretaceous series from the SSZ. (e) Isolated klippen of SSZ marbles and amphibolites resting on top of the colored melange between Ab Dasht and Bidou (Figure 2a). (f) Folded Cretaceous limestone wrapping the incipiently metamorphosed colored melange west of Seghina. Their position in the nappe pile is shown on the section of Figure 2d. (g) Well-preserved pillow lavas in the incipiently metamorphosed colored melange west of Seghina. (h) Typical chaotic aspect of the colored melange far from BS exposures: serpentinites, radiolarites and pelagic limestone beds crop out in a completely disorganized fashion which contrasts with the highly schistosed BS exposures.

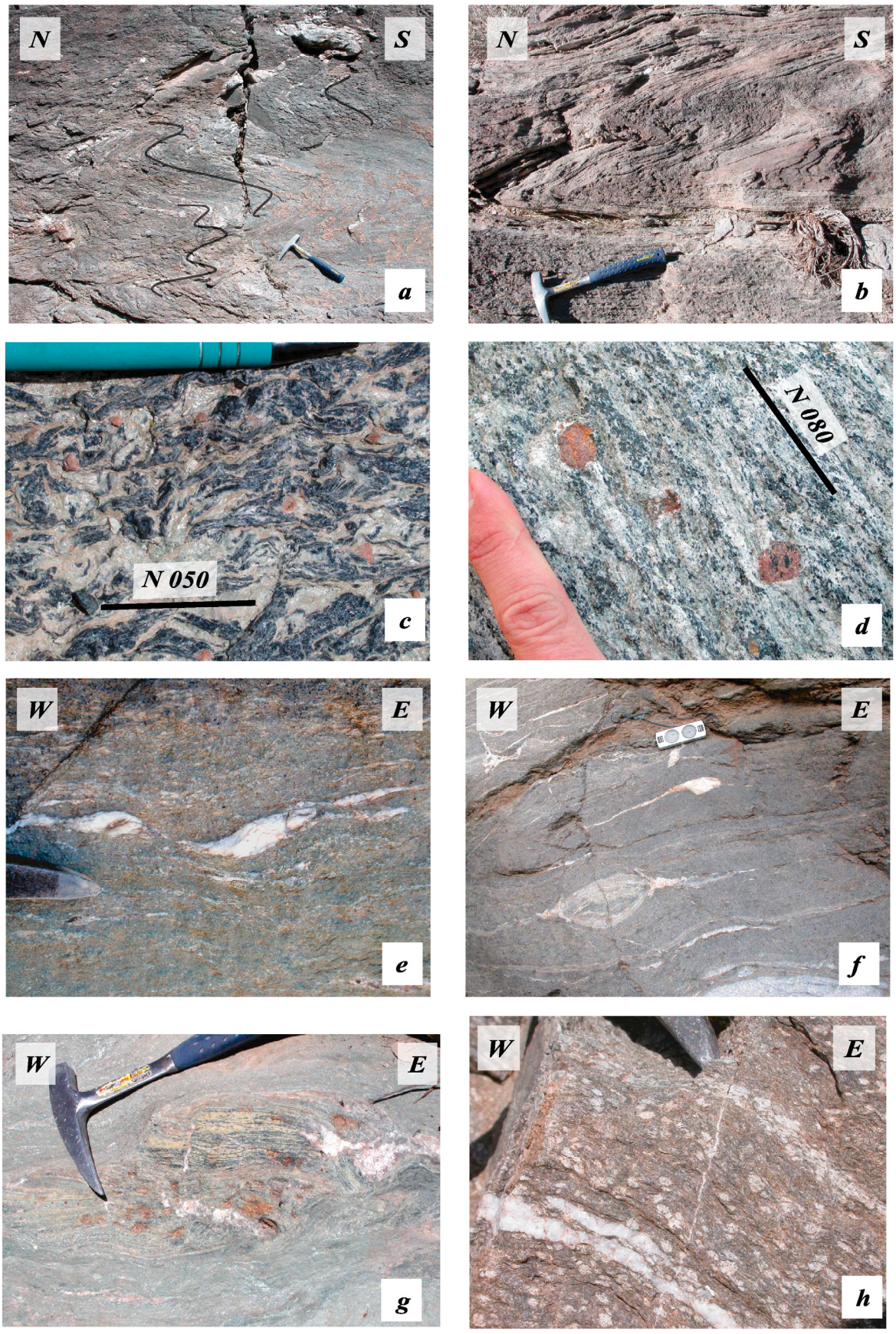

Figure 5

Table 1. Parageneses of the Main Samples Studied in SE Zagros[a]

Sample	Qz	Cc	Phg	Chl	Bt	Gt	Am	Ep	Pl	Cpx	Lws	Kf	Rt	Ti	Ap	Area	Data	GPS Coordinates North	GPS Coordinates East
3.01a[b,c]	x	x	x	x		x	x	x				x		x		Ashin	D	28°29′26″	56°58′41″
3.01b[b]	x	x	x	x		x							x	x		Ashin	P	28°29′26″	56°58′41″
3.04a[c]	x	x	x	x			x									Seghina	D	28°23′21″	56°48′10″
3.04b[b,c]	x	x	x	x			x	x	x			x		x		Seghina	D + P	28°23′21″	56°48′10″
3.12b[b,c]	x		x	x		x		x	x				x			Ashin	D+P	28°29′44″	56°58′06″
3.12d[b]	x		x	x	x	x	x	x	x				x		x	Ashin	P	28°29′44″	56°58v06″
3.16b	x		x	x		x										Ashin	R	28°30′00″	56°59′12″
3.27a[b,c]	x		x	x		x		x	x						x	Sheikh Ali	D + P	28°10′02″	56°49′35″
3.27b[b]	x	x	x	x				x	x				x	x		Sheikh Ali	P	28°10′02″	56°49′35″
3.28a[b,c]	x		x	x		x			x				x			Sheikh Ali	D+P+R	28°10′05″	56°49′40″
4.07a	x		x	x	x	x	x		x				x	x		Ashin	R	28°27′49″	56°55′26″
4.09a[b]	x	x	x	x		x	x	x	x			x	x			Ashin	P	28°29′23″	56°57′05″
4.19b	x	x	x	x		x		x					x	x	x	Ashin	R	28°30′35″	56°59′23″
4.20a[b]	x	x	x				x			x	x		x	x		Seghina	P	28°29′47″	56°52′59″
4.28a[b]	x	x	x	x			x	x	x			x	x	x		Sheikh Ali	P	28°05′64″	56°45′40″
4.28b	x		x	x		x		x	x				x	x		Sheikh Ali	R	28°05′64″	56°45′40″
4.35c[b]	x	x	x	x		x	x	x	x				x	x		Ashin	P	28°31′48″	57°02′28″
4.36a	x	x	x	x		x		x	x				x	x		Ashin	R	28°29′11″	56°54′55″
4.36b[b]	x	x	x	x		x		x	x				x			Ashin	P+R	28°29′11″	56°54′55″
4.37b[b]	x		x	x	x	x	x	x	x					x	x	Ashin	P	28°29′14″	56°55′09″
4.40b[b]	x	x	x	x				x	x				x			Hajiabad	P	28°22′44″	56°12′09″
4.42b[b]	x		x	x			x	x					x			Shadab	P	28°13′50″	56°32′05″
4.44a[b]	x	x	x	x			x	x						x		Shadab	P	28°13′39″	56°32′13″

[a]D, samples selected for radiomatric dating (Figure 9b and Table 4); P, samples for which electron probe microanalyses were obtained (e.g., Table 2); R, samples used for Raman (Figure 8c). Mineral abbreviations are Qz, quartz; Cc, calcite; Phg, phengite; Chl, chlorite; Bt:biotite; Gt, garnet; Am, amphibole; Ep, epidote; Pl, plagioclase; Kf, K feldspar; Rt, rutile; Ti, titanite; Ap, apatite. The x means that the mineral is present. Samples were used for Raman spectroscopy or a combination of them unless otherwise noted.
[b]Samples were probed.
[c]Samples were dated.

compositions ($Al/Al+Fe^{3+} > 0.5$). Biotite appears in sample 3.12d as an inclusion in garnet, and in sample 4.37b. Its composition lies along the tschermak substitution line between eastonite and phlogopite/annite with Si^{4+} = 2.75–2.8 and X_{Mg} = 0.45. Plagioclase normally is purely albitic in composition except in sample 3.12b where 4–5% of anorthite component is present.

4. P-T Constraints

4.1. Methods

4.1.1. Estimation of P-T Conditions

[35] In as much as the major source of errors in P-T estimates stems from the definition of equilibrium parageneses, we combined criteria such as the habit of minerals, their textural relationships, and microstructural location to select minerals for multiequilibrium calculation purposes. Selected minerals involved in the same microstructural domain and in close contact are regarded to have crystallized coevally. In parageneses involving garnet, minerals in the pressure shadows were assumed to be in equilibrium with the garnet rim composition.

4.1.1.1. THERMOCALC Thermobarometry

[36] Calculations used the internally consistent thermodynamic data set of *Holland and Powell* [1998] and the program THERMOCALC v3.21 [*Holland and Powell*, 1990, 1998]. Recalculation of the analyses, including the calculation of Fe^{3+} iron and mineral end-member activities was performed with the program AX, of Holland and Powell (ftp://www.esc.cam.ac.uk/pub/minp/AX/).

[37] Only P-T estimates satisfying the equilibrium test criteria (e.g., sigfit, hat [*Holland and Powell*, 1998]) have been considered in this study (Figure 8). Accuracy on the P-T estimates, estimated by the error ellipse parameters, is typically of the order of 10–30°C for temperature and 1–2 kbar for pressure. Some end-members present only in small amounts, such as amesite for chlorite (Figure 7e), which produce a large uncertainty on the results, were removed (see Table 2).

4.1.1.2. TWEEQU Multiequilibrium Thermobarometry

[38] This multiequilibrium approach of *Berman* [1991] [*Vidal and Parra*, 2000] was chosen for a number of samples in order to get other independent P-T estimates to be compared with those of THERMOCALC. P-T estimates were calculated with TWEEQU 2.02 software [*Berman*, 1991] and its associated database JUN92 complemented by thermodynamic properties for Mg-amesite, Mg-sudoite, Mg-celadonite and chlorite and phengite solid solution models from *Vidal and Parra* [2000], *Vidal et al.* [2001] and *Parra et al.* [2002]. The temperature (σT) and pressure

Figure 5. (a) Recumbent folds in Ashin blueschists highlighting the importance of flattening during greenschist facies metamorphism (underlined by quartz-chlorite veins). (b) Recumbent folding in marbles near Ashin. (c) Iron-rich blue amphiboles oriented along a discrete lineation trend. (d) Garnet-blue amphibole micashist showing an E-W lineation trend. (e) Stretched veins indicating a top to the east shear sense. (f) Stretched veins advocating for coaxial stretching and boudinage. (g) Stretched glaucophane-epidote-rutile-bearing boudin in a fine-grained GS facies matrix. (h) Albite-rich, GS facies gneiss.

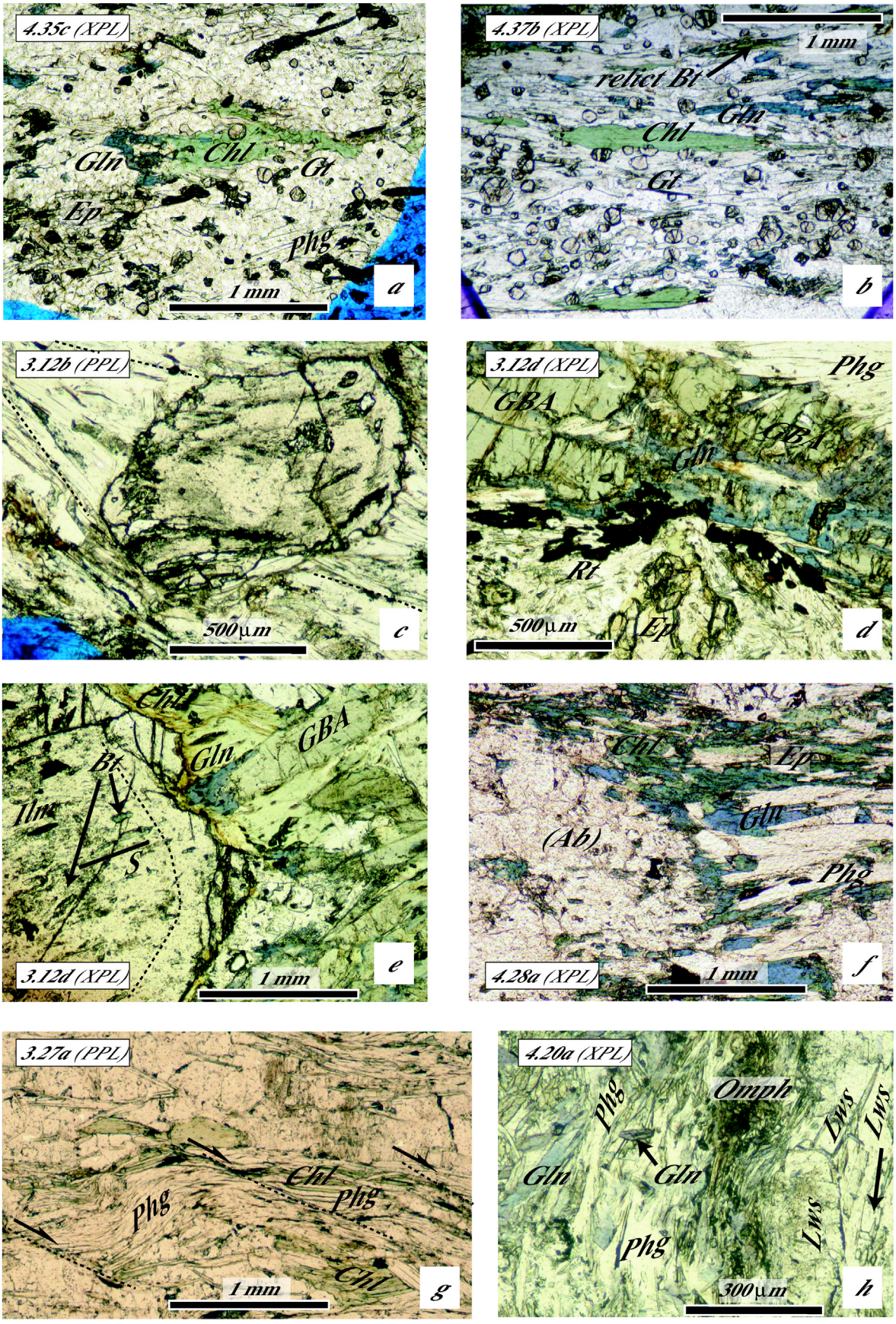
4.35c (XPL)
Gln
Chl
Gt
Ep
Phg
1 mm
a
4.37b (XPL)
1 mm
relict Bt
Gln
Chl
Gt
b
3.12b (PPL)
500 µm
c
3.12d (XPL)
Phg
GBA
GBA
Gln
Rt
500 µm
Ep
d
Chl
GBA
Gln
Bt
Ilm
S
3.12d (XPL)
1 mm
e
Chl
Ep
Gln
(Ab)
Phg
4.28a (XPL)
1 mm
f
3.27a (PPL)
Phg
Chl
Phg
Phg
1 mm
Chl
g
4.20a (XPL)
Phg
Omph
Lws
Lws
Gln
Gln
Lws
Phg
300 µm
h

Figure 6

(σP) scatter were calculated with INTERSX [*Berman*, 1991]. If σP > 800 bar or σT > 25 °C [*Vidal et al.*, 2001; *Parra et al.*, 2002] the minerals are considered to be out of equilibrium and the P-T estimates are rejected.

4.1.2. Estimation of Peak Temperatures

[39] The Raman spectroscopy of carbonaceous material (RSCM [*Beyssac et al.*, 2002]) was calibrated as a geothermometer (±50°C) in the range 330–650°C. Relative, intersample uncertainties on temperature can be much smaller, around 10–15°C [*Beyssac et al.*, 2004]. Since the degree of organization of the carbonaceous material is irreversible, temperatures deduced from the Raman spectra represent peak temperature conditions reached by the rocks. RSCM was done on thin sections of graphite-bearing schists oriented perpendicular to the foliation by focusing the laser beam beneath a transparent crystal. Raman spectra were obtained with a Renishaw INVIA Reflex Raman microspectrometer at the Laboratoire de Géologie of the Ecole Normale Supérieure, Paris, France. Spectra were excited at room temperature with the 514.5 nm line of a 20 mW Ar Spectra Physics laser through a LEICA 100X objective (NA 0.90). The laser beam is depolarized before the microscope thanks to a 1/4 λ wave plate. The laser spot on the surface had a diameter of approximately 1 μm and a power of 1 mW, which should be low enough to avoid any spectral change or sample destruction due to light absorption and local temperature increase [e.g., *Beyssac et al.*, 2003]. Light was dispersed by a holographic grating with 1800 grooves mm^{-1}. A spectral resolution of about 1.4 cm^{-1} was determined by measuring a Neon lamp emission. The spectrometer is calibrated for every session by measuring the position of the neon lamp emission and/or a silicon wafer. The dispersed light was collected by a RENCAM CCD detector. Confocality was achieved by setting the entrance slit into the spectrometer to 11 μm and selecting via the software few relevant rows on the CCD creating a ''virtual'' pinhole. The depth resolution of this confocal configuration is less than 2 μm. The synchroscan mode from 700 to 2000 $cm-^{1}$ was selected in order to avoid step-like mismatches between neighboring spectral windows probably occurring in samples with intense and uneven background and to maximize the signal-to-noise ratio. Acquisition duration was 60s divided in three 20s substractive runs. We recorded at least 8 spectra for each sample to take into account the CM heterogeneities. The program Peak Fit 4.0 was then used to process the spectra.

4.2. Results

[40] P-T estimates were performed with THERMOCALC for 10 samples. Some of the calculations are given in Table 3 (and corresponding analyses in Table 2). Results for Ashin and Sheikh Ali are presented on Figures 8a and 8b. Peak burial P-T conditions for Gt-Phg-Chl-Rt±Ep±Amph±Ti±Bt assemblages cluster around 520–530°C for 11 kbar on average, with some samples yielding slightly higher-grade P-T estimates, at around 12 kbar (±0.5) and 570 °C (±10; samples 3.12b, 3.27a, 4.36b). These P-T estimates are consistent with the frequent lack of jadeite and with parageneses expected from pseudosections [*Schmädicke and Will,* 2003, Figure 7a] calculated for compositions close to Hajiabad BS [*Sabzehei*, 1974, pp. 217, 228]. P-T estimates for the Lws-Omph-Gln-Phg assemblage of Seghina (Figure 8b) point to higher-P conditions between 17 and 18 kbar at 500°C, in agreement with the P-T grid published by *Wei et al.* [2003] and *Wei and Powell* [2006].

[41] The P-T estimates obtained with TWEEQU broad accord with those of THERMOCALC (e.g., compare 3.28a and 4.28a) but yield somewhat lower temperatures at peak pressure conditions (e.g., sample 4.36b). RSCM temperatures (Figure 8c) range between 460° ± 7 and 537° ± 9, with an average value of 515°C ± 19 for Ashin. Maximum RSCM temperatures are somewhat lower on average (~20°C) than temperatures estimated with THERMOCALC, but the discrepancy remains within the bounds of the RSCM calibration (± 50°C [*Beyssac et al.*, 2002]) and there is a good fit for samples for which both the RSCM temperature and the peak P-T estimates are available (3.28, 4.28a, 4.36b; Figures 8c and 8d). These P-T estimates are within (but on the high-T side of) the BS facies stability fields defined by *Evans* [1990] for blue amphiboles of similar composition (Figure 8d). Maximum burial P-T estimates for the majority of samples define a metamorphic P-T gradient of 15°C km^{-1} (Figure 8e).

[42] Our results point to slightly different exhumation P-T paths. Core to rim zonations in garnets, in samples such as 3.01b and 3.12b, are consistent with a slight increase of temperature (~40–50°C). This temperature increase is accompanied by a slight pressure increase for the former and a slight pressure decrease for the latter, although the uncertainties on pressure for the two estimates overlap. This slight heating is consistent with the observation that at least some of the samples partly enter into the epidote amphibolite facies on exhumation. In contrast, other samples from Sheikh Ali (samples 3.28a, 4.28a) show a P-T evolution characterized by cooling on decompression (and a sudoite content increase in the chlorite; Figure 7e).

[43] Garnet zonation profiles (Figure 7f), due to changing minerals equilibrating with garnet and/or due to subtle temperature variations, point to somewhat more complex

Figure 6. Microphotographs of some of the samples investigated in the present study (PPL, plane polarized light; XPL, cross-polar light). Ab, albite; Bt, biotite; Chl, chlorite; GBA, greenish blue amphibole; Gln, glaucophane; Gt, garnet; Ilm, ilmenite; Lws, lawsonite; Omph, omphacite; Phg, phengite; Rt, rutile. (a–b) Gt-Chl-Gln-Phg-Ep assemblages. (c) Asymmetric pressure shadows (underlined by dashed contours) around garnet in a quartz-chlorite-phengite-rich matrix. The garnet crystal shows a prograde rim overgrowth which partly reacted back during the retrograde path. (d) Blue amphibole growing at the expense of greenish blue amphibole (see Figure 7b) together with rutile and epidote. (e) Blue amphibole overgrowths on GBA in equilibrium with the garnet rim and chlorite. Biotite inclusions, which belong to an ancient schistosity (S) also underlined by ilmenite, are visible in garnet. Garnet core compositions (see the profile of Figure 7f) are in equilibrium with GBA and biotite (Table 3 and Figure 8a). (f) Ep-Chl-Gln-Phg pressure shadow around an albite porphyroblast. (g) Greenschist facies chlorite-phengite schistosity and shear bands (dashed lines). (h) Lws-Gln-Omph-Phg metabasite near Seghina.

P-T paths but more work is needed and mineral inclusions in garnet are scarce. Biotite inclusions in garnet from metabasite 3.12d, which equilibrated with the garnet core and sodi-calcic amphiboles hosted in the garnet, are nevertheless useful to constrain the prograde path. Comparing P-T estimates between the early Gt_{core} greenish blue amphibole-biotite and late Gt_{rim}-glaucophane-phengite-chlorite estimates suggest that burial was accompanied by a moderate pressure increase from 7 kbar/470°C to 10 kbar/530°C. Biotite and greenish blue amphibole relics in sample 4.37b yield a similar prograde path (Figure 8a).

5. Radiometric Constraints

5.1. Analytical Procedure

[44] The ^{40}Ar-^{39}Ar in situ laser ablation technical procedure was first proposed by *Schaeffer et al.* [1977], modified by *Maluski and Monié* [1988], and was recently detailed elsewhere [*Agard et al.*, 2002]. We recall here the main stages for ^{40}Ar-^{39}Ar in situ sample preparation and analytical procedure. The laser system consists of (1) a continuous 6w argon ion laser, (2) a beam shutter for selection of lasering exposure time, with typically 5 ms pulses separated by 40 ms, and (3) a set of lenses for beam focusing. The number of pulses depends on the nature of the analyzed mineral, its K content and its presumed age. Argon extraction, purification and analyses are performed within three distinctive parts with (4) the sample chamber where gas extraction is done, (5) the purification line with hot getters and nitrogen liquid traps (cold) traps, and (6) a MAP 215-50 noble gas mass spectrometer equipped with an electron multiplier.

[45] Rock sections of 1 mm thick, which had been used to make the petrographic thin sections, were double polished within 1 μm tolerance. Whole section and detailed area photographs of both the rock section and corresponding thin section were taken for an accurate selection of favorable areas during lasering experiments. All samples were ultrasonically rinsed in ethanol and distilled water, wrapped in pure aluminum foils and then irradiated in the McMaster nuclear reactor (Canada) with several aliquots of the MMHb-1 international standard (520.4 ± 1.7Ma [*Samson and Alexander*, 1987]. After irradiation, both the monitors and the sections were placed on a Cu holder inside the sample chamber and heated for 48 hours at 150–200°C.

[46] For each age determination, argon was extracted from a 150 × 300 μm surface which always corresponds to a mixture of several phengite grains taking into account the small size of the grains (Figure 9a). The crater is a 30–40 μm approximate hemisphere surrounded by a circular wall made of melted material. Incision of the sample did not exceed 10–20 μm deep depending on the three-dimensional orientation of the phengite crystals.

[47] Once the extraction was completed, about four minutes were required for gas cleaning of the line and 15 min for data acquisition by peak jumping from mass 40 to mass 36 (8 runs).

[48] For each experiment, ages have been obtained after correction with blanks, mass discrimination, radioactive decay of ^{37}Ar and ^{36}Ar and irradiation-induced mass interferences. They are reported with one sigma uncertainty (Table 4) and were evaluated assuming an atmospheric composition for the initially trapped argon (i.e., $(^{40}Ar$-$^{36}Ar)^{i}$ ~295.5).

5.2. Results

[49] Radiometric ages range between 82.3 and 126.5 Ma (Figure 9b and Table 4). Individual samples span the range 82–102 and 89–109 Ma for Ashin, 95–126 Ma for Seghina, and 87–102 and 116–118 Ma for samples from Sheikh Ali. When only considering samples from Ashin and sample 3.28a from Sheikh Ali, the average age value is 93.0 Ma ± 5.9 (Table 4 and Figure 9c). Results for Seghina point to slightly older ages than for Ashin (112.4 ± 10.6; Table 4). These ages are somewhat scattered, but less so when considering individual samples (Table 4).

[50] As mentioned before, our samples, mostly taken from preserved BS boudins, preserve few key syntectonic textural features (contrary to *Agard et al.* [2002] and *Augier et al.* [2005], for example). In detail, however, some samples show that the ages obtained respect the relationship between structural/textural site and age. The example of sample 3.01-S6 shows that phengite grains from the schistosity yield ages between 96 and 88 Ma (Figure 9a), whereas younger ages on average (circa 91–84 Ma) are present along later, crosscutting shear bands. Older ages

Figure 7. Mineral plots of compositions determined with the electron probe microanalysis. XMg is hereinafter taken as Mg/Mg+Fe. (a) Na (site B) versus Si content in all the SE Zagros amphiboles analyzed in this study. Compositions mainly cluster in the glaucophane field and around a composition intermediate between magnesiohornblende and barroisite but span the entire range. Terminology is after *Leake et al.* [1997]. (b) Evolution trend of the successive amphibole generations, from sodi-calcic, greenish blue amphiboles to blue amphiboles for three samples. (c) Evolution trend of blue amphibole with time toward glaucophane-rich compositions (samples 4.20a, 4.35c, 4.44a) in the classical glaucophane-crossite-riebeckite diagram. (d) Phengite composition variations, which are mostly parallel to the muscovite-celadonite (Mus-Cel) joint. The variations are dominated by the tschermak substitution exchange vector Si(Mg,Fe)-2Al as for most blueschist facies rocks. Note that phengite from sample 4.20a reach exceptionally high tschermak values (Si^{4+} = 3.7; see also Table 2). (e) Chlorite plot mostly along the amesite-clinochlore (Ames-Clin) joint as a result of the tschermak substitution. Some significant deviations toward sudoite (Sud) are observed for late chlorite in samples from Sheikh Ali (3.27a, 3.28a). (f) Triangular plot. Garnet compositions are expressed as a function of their grossular, pyrope, and almandine content (Grs-Pyr-Alm, respectively, i.e., as a function of their Ca-Fe-Mg content). Thick gray lines indicate core to rim evolution of the composition observed in the garnet profiles of samples 3.01b, 3.12d, 3.27a given below. Garnet profiles show a coherent decrease of Mn and Ca and an increase of Fe and Mg (and of the XMg) toward the rim. This evolution is less pronounced for sample 3.12d. Sample 3.01b also shows second-order zonation patterns.

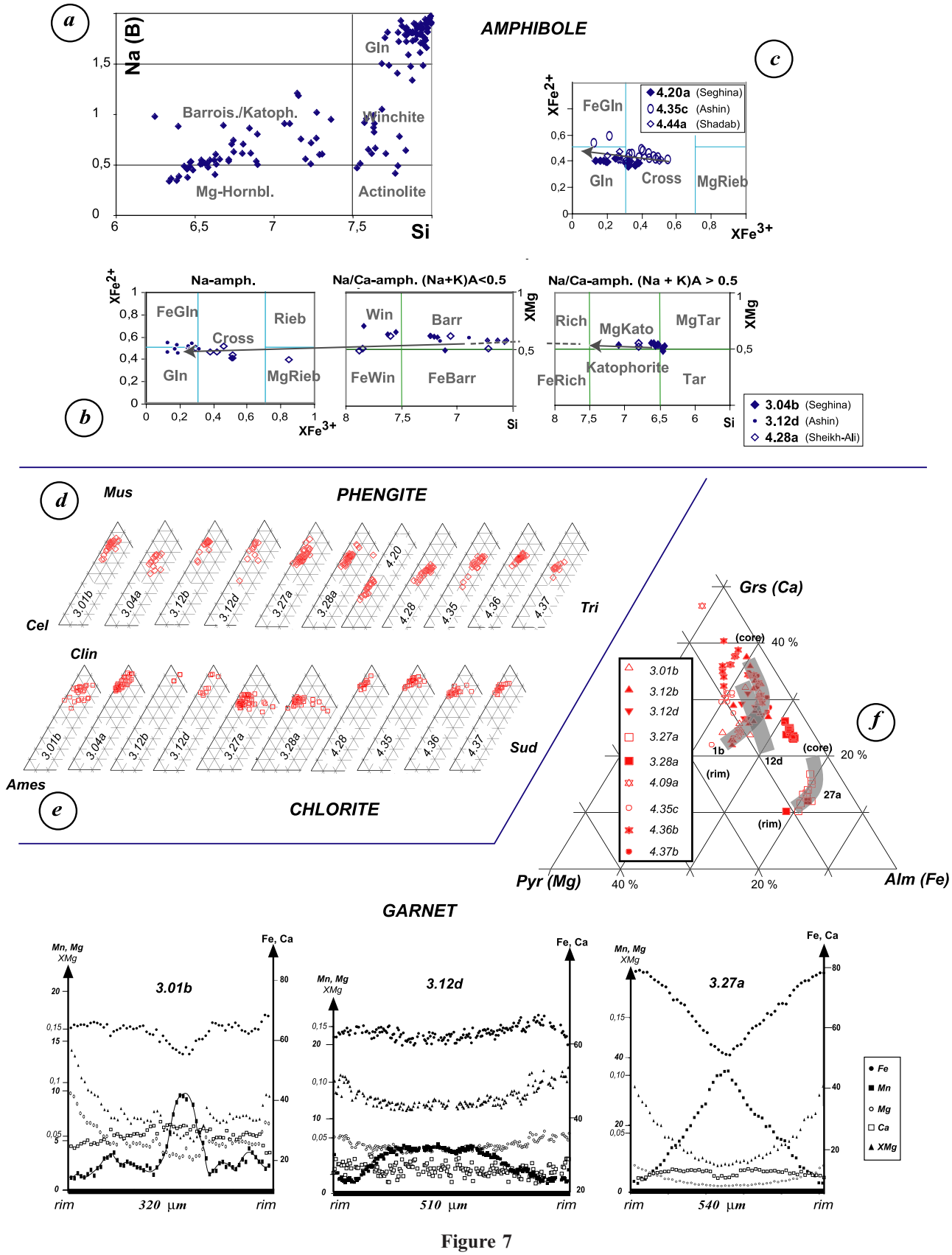
a
Na (B)
Si
Gln
Barrois./Katoph.
Winchite
Mg-Hornbl.
Actinolite
AMPHIBOLE
c
XFe2+
XFe3+
FeGln
Gln
Cross
MgRieb
4.20a (Seghina)
4.35c (Ashin)
4.44a (Shadab)
b
Na-amph.
Na/Ca-amph. (Na+K)A<0.5
Na/Ca-amph. (Na + K)A > 0.5
FeGln
Gln
Cross
Rieb
MgRieb
Win
Barr
FeWin
FeBarr
Rich
MgKato
MgTar
FeRich
Katophorite
Tar
XMg
Si
3.04b (Seghina)
3.12d (Ashin)
4.28a (Sheikh-Ali)
d
Mus
PHENGITE
Cel
Tri
Clin
Sud
Ames
e
CHLORITE
3.01b
3.04a
3.12b
3.12d
3.27a
3.28a
4.20
4.28
4.35
4.36
4.37
f
Grs (Ca)
Pyr (Mg)
Alm (Fe)
40 %
20 %
(core)
(rim)
1b
12d
27a
3.01b
3.12b
3.12d
3.27a
3.28a
4.09a
4.35c
4.36b
4.37b
GARNET
Mn, Mg
XMg
Fe, Ca
3.01b
3.12d
3.27a
rim
320 µm
510 µm
540 µm
Fe
Mn
Mg
Ca
XMg

Figure 7

(circa 91–90 Ma) along the shear bands could result from excess argon or to incomplete recrystallization.

[51] This age scatter could be accounted for by the presence of excess argon in these high-pressure rocks, as shown in a number of case studies [e.g., *Arnaud and Kelley*, 1995; *Scaillet*, 1996; *Giorgis et al.*, 2000; *El-Shazly et al.*, 2001]. It should also be realized that several grains had to be fused during each experiment to get a sufficient signal/noise ratio and contamination cannot be ruled out. These age data should therefore be considered as preliminary constraints. On the other hand, the relative intersample consistency of the data shows that excess argon, if any, has probably only induced relatively minor, second-order age modifications. We note that these ages are in agreement with the only other radiometric K/Ar ages published so far of 79.0 ± 1.5 and 82.4 ± 1.4 Ma on Ashin mica schists [*Ghasemi et al.*, 2002].

[52] P-T paths suggest that crystallization temperatures of phengite were higher than the commonly accepted closure T for this mineral (~350–430 °C [e.g., *Villa*, 1998]), even if this temperature range is still debated [*Agard et al.*, 2002, and references therein]. Hence one should expect all ages to be similar. Figures 9b and 9c, showing that most ages lie within the range 95–85 Ma, suggest that this might have been the case but that the pattern was later modified. The observed scatter could result from a combination of (1) minor excess argon later, (2) deformation-related reequilibrations, (3) slightly discordant exhumations, and/or (4) contamination by minerals adjacent to phengite. A simple interpretation of the data could be that all samples from Ashin and sample 3.28a from Sheikh Ali crossed the closure temperature between approximately 95 and 85 Ma, and were contaminated to a variable extent by excess argon or suffered argon loss during more recent tectonic activity. These ages are preliminary and ought to be complemented by step heating age determinations on single grains. They show, however, that BS facies rocks had returned to midcrustal depths <15–20 km (i.e., T < 350–430°C) before 80 Ma.

6. Discussion

6.1. Petrological Results

[53] Our study demonstrates the existence of glaucophane in Zagros and the presence of highly substituted phengite (Si^{4+} = 3.3–3.5 and up to 3.7; Table 2). Maximum burial P-T estimates cluster around 10–11 kbar and 520–530°C for most samples, along a metamorphic P-T gradient of 15°C km^{-1} (Figure 8e). Most BS samples therefore equilibrated at depths around 35–40 km, contrary to the melange of the east Iran Sistan suture zone [*Fotoohi Rad et al.*, 2005]. One significant exception is the lawsonite-omphacite-bearing BS encased in matrix serpentinite (Seghina area), which equilibrated at ~17–18 kbar and 500°C, in the lawsonite-eclogite field defined by *Wei et al.* [2003]. No proper garnet-omphacite-bearing eclogites were found however.

[54] The prograde path partly preserved in samples 3.12d and 4.37b could represent either an earlier metamorphic imprint or an equilibration stage during burial, but more work is needed before this can be assessed. In the latter case, this nearly isothermal burial (Figure 8e) could correspond to a cooling of the subduction thermal regime in response to increased convergence velocities (see below), as proposed for the progressive cooling of the subduction regime in the Catalina series [*Peacock*, 1990; *Grove and Bebout*, 1995] or in the Coastal Cordillera accretionary complex of Chile [*Willner et al.*, 2004].

[55] Exhumation P-T paths point to different return conditions, with a slight heating for Ashin and an isothermal to cooling return path for Sheikh Ali and Seghina. As a first approximation, age data suggest that the Hajiabad blueschists studied here crossed the closure temperature more-or-less coevally, between 95 and 85 Ma, and were contaminated by minor excess argon (see above discussion; Figure 9b). Exhumation velocities could not be calculated for individual samples but a first-order constraint can be inferred: assuming that ages for sample 3.01b are representative of the average BS to GS retrograde history (from circa 95 to 85 Ma; Figure 9a), pressure conditions for the BS would have decreased from 11–12 kbar to 5–6 kbar (Figure 8e) in approximately 10 Ma. This corresponds to exhumation velocities on the order of 1.5 mm yr^{-1}.

[56] These blueschists were largely exhumed before 80 Ma (Figure 8e), long before the end of subduction (circa 35 Ma) and the onset of collision: exhumation therefore took place during oceanic convergence, as for the HP-LT rocks from Margarita island or Cuba [*Stöckhert et al.*, 1995; *Schneider et al.*, 2004]. Cold return P-T paths (e.g., samples 3.28a, 4.28a; Figure 8b) are consistent with synconvergence exhumation [e.g., *Ernst*, 1988; *Agard et al.*, 2001] and exhumation velocities about 1–2 mm yr^{-1}, if confirmed, are comparable with synconvergence BS exhumation rates in the Alps [*Agard et al.*, 2002]. Exhumation patterns dominated by flattening and orogen-parallel extension in Zagros BS point to wedge dynamics with active underplating processes, as described by *Platt* [1993, 2000, Figure 10b]

Figure 8. P-T plots showing the results of our P-T estimates using THERMOCALC (Tc [*Holland and Powell*, 1990, 1998]) or TWEEQU (Tw [*Berman*, 1991]) and estimates of maximum temperatures with the Raman spectroscopy of carbonaceous material (RSCM [*Beyssac et al.*, 2002, 2004]). Ellipses indicate confidence intervals obtained with THERMOCALC. Confidence intervals obtained with TWEEQU (Intersx program [*Berman*, 1991]) lie within the dotted bounds (small error bars on each P-T constraint). (a) Results for Ashin samples. (b) Results for Sheikh Ali and Seghina samples. (c) RSCM temperatures, which represent the peak temperatures reached by the samples, calibrated with a precision of ~50°C [*Beyssac et al.*, 2002]. (d) All P-T results plotted versus RSCM temperatures. The blueschist (BS) stability fields for the glaucophanitic and crossitic compositions 4 and 6 of *Evans* [1990], which are close to those measured in the present study, are indicated. The position of the albite = jadeite+quartz reaction (Ab = Jd+Qz) is also recalled. Same symbols for P-T estimates as in Figures 8a and 8b. (e) Synthetic P-T paths for Hajiabad blueschists. Average peak P-T estimates correspond to a metamorphic P-T gradient of ~15°C km^{-1}, except for Lws-Cpx-Gln-Phg assemblages of Seghina (sample 4.20a). These maximum burial conditions were reached during the period 95–85 Ma (see Figure 9b and discussion for details). The blueschists crossed the closure temperature of phengite (~350°C [*Villa*, 1998]) before 80 Ma.

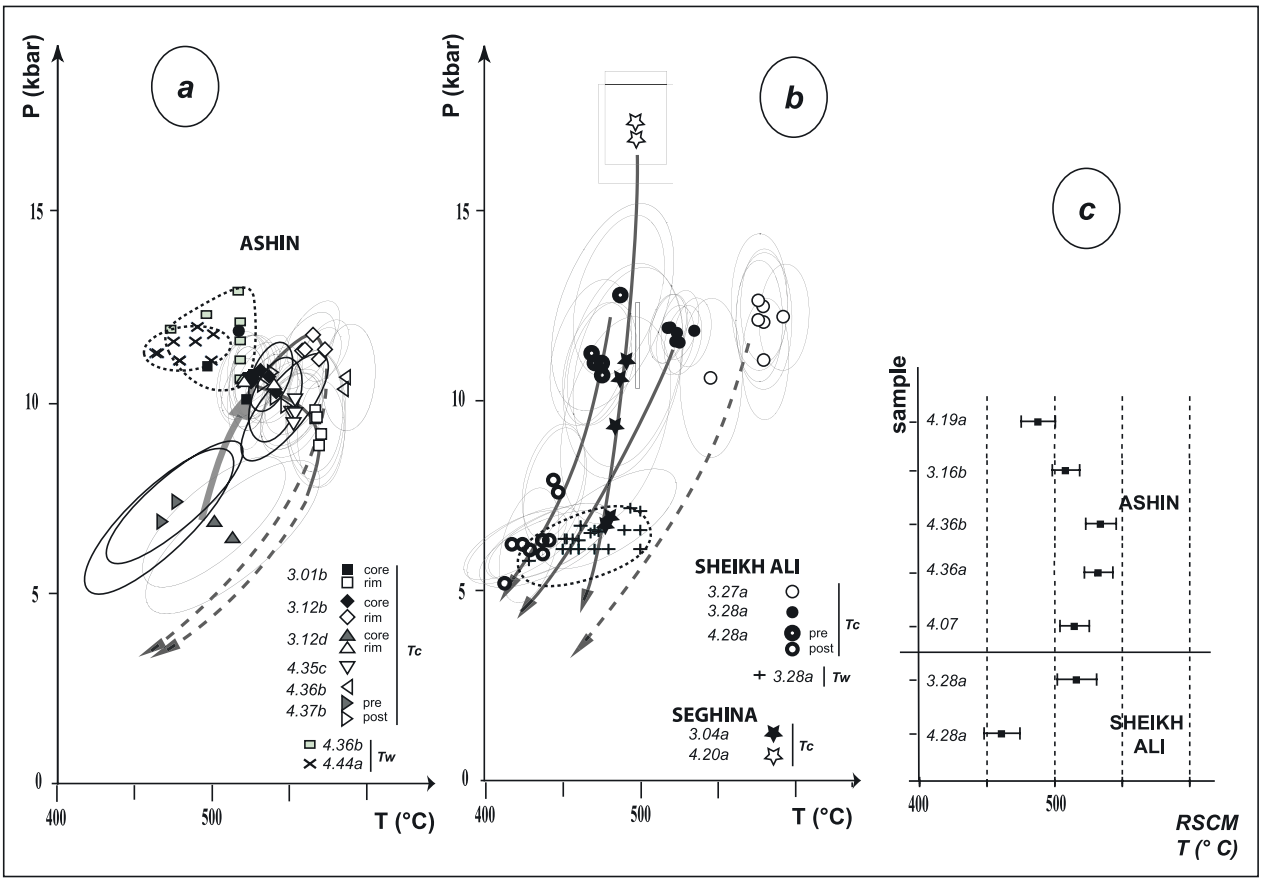
a
P (kbar)
ASHIN
3.01b core rim
3.12b core rim
3.12d core rim
Tc
4.35c
4.36b
4.37b pre post
4.36b
4.44a
Tw
T (°C)
b
SHEIKH ALI
3.27a
3.28a
4.28a pre post
Tc
3.28a Tw
SEGHINA
3.04a
4.20a
Tc
c
sample
4.19a
3.16b
ASHIN
4.36b
4.36a
4.07
3.28a
4.28a
SHEIKH ALI
RSCM T (° C)

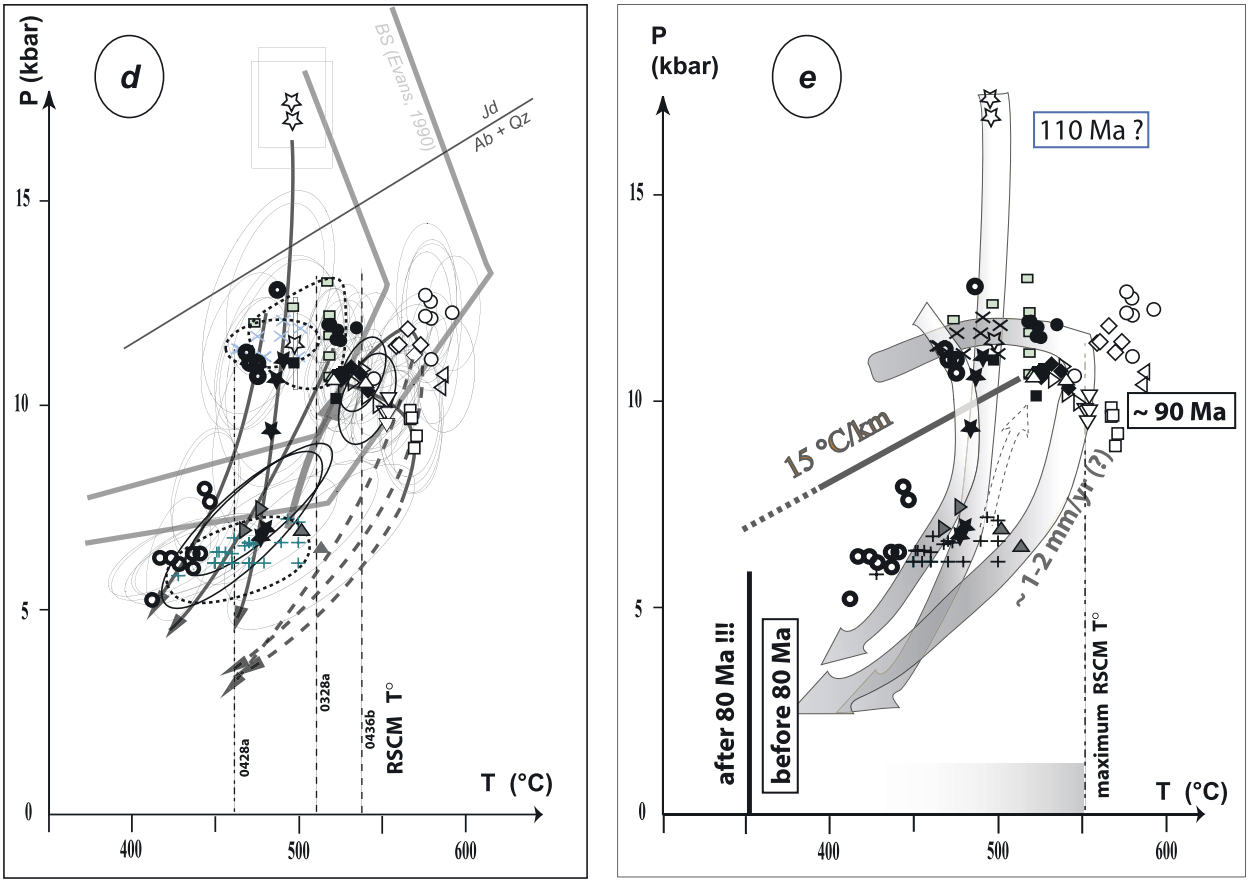
d
P (kbar)
BS (Evans, 1990)
Jd
Ab + Qz
0428a
0328a
0436b
RSCM T°
T (°C)
e
P (kbar)
110 Ma ?
~ 90 Ma
15 °C/km
~ 1-2 mm/yr (?)
after 80 Ma !!!
before 80 Ma
maximum RSCM T°
T (°C)

Figure 8

Table 2. Representative Analyses of the Main Mineral Groups Found in Hajiabad Blueschists[a]

	amp								cpx		lws	ep			g								
	3.04b	3.04b	3.12d	3.12d	3.12d	4.28a	4.28a	4.35c	4.20	4.20	4.20	3.04b	3.12b	4.28a	3.01b	3.01b	3.12b	3.12b	3.12d	3.12d	3.27a	3.28a	4.35c
Analysis	d124	d62	ag11	ag12	ag58	w10	w69	aa109	b16	b23	b28	d45	c88	w34	c43	c46	c75	c120	ag28	ag51	c238	ag294	w95
SiO_2	56.69	49.45	56.52	44.05	45.64	55.86	46.39	57.24	55.76	57.36	39.41	37.75	38.90	37.53	38.12	37.90	38.22	37.64	37.52	37.93	36.63	36.89	37.74
TiO_2	0.00	0.12	0.24	0.39	0.39	0.18	0.25	0.09	0.10	0.07	0.07	0.07	0.12	0.07	0.08	0.18	0.00	0.19	0.16	0.17	0.00	0.05	0.15
Al_2O_3	5.19	6.11	10.71	15.51	13.20	6.72	9.72	5.66	10.93	10.49	31.66	25.50	28.08	22.70	21.88	21.18	22.09	21.28	20.80	21.16	21.08	20.86	20.78
FeO	18.72	18.30	15.37	14.07	14.67	18.75	19.87	18.29	15.86	15.33	0.54	9.42	6.74	14.48	28.21	28.10	29.16	22.05	29.09	28.09	36.30	26.81	23.59
MnO	0.21	0.24	0.08	0.19	0.22	0.07	0.26	0.52	0.03	0.15	0.00	0.07	0.01	0.49	0.84	1.55	0.87	8.66	2.78	2.29	1.40	7.07	8.13
MgO	9.43	11.15	7.51	10.02	10.44	7.92	9.22	7.67	1.26	2.84	0.00	0.02	0.03	0.02	3.30	1.04	3.23	0.64	1.47	2.15	2.27	0.64	1.75
CaO	2.09	9.52	1.25	10.38	10.27	0.99	8.25	1.05	2.71	2.72	17.86	22.98	23.02	22.41	8.54	10.61	7.73	10.18	9.23	9.08	3.43	7.65	8.81
Na_2O	6.48	2.43	6.73	2.20	2.25	6.74	4.04	6.32	13.02	11.94	0.02	0.01	0.06	0.01	0.00	0.02	0.00	0.02	0.02	0.03	0.05	0.05	0.00
K_2O	0.03	0.27	0.04	0.34	0.36	0.06	0.45	0.00	0.00	0.00	0.00	0.01	0.02	0.00	0.00	0.01	0.00	0.00	0.05	0.02	0.01	0.00	0.00
S	98.81	97.59	98.43	97.14	97.46	97.29	98.44	96.83	99.66	100.89	89.53	95.84	96.98	97.70	100.98	100.59	101.31	100.64	101.12	100.91	101.17	100.02	100.95
												Structural formula											
Si	8.10	7.35	7.91	6.48	6.70	8.08	6.93	8.28	2.07	2.09	2.04	3.08	3.08	3.09	2.98	3.01	2.98	2.99	2.98	3.00	2.95	2.98	3.00
Ti	0.00	0.01	0.02	0.04	0.04	0.02	0.03	0.01	0.00	0.00	0.00	0.00	0.01	0.00	0.00	0.01	0.00	0.01	0.01	0.01	0.00	0.00	0.01
Al	0.87	1.07	1.77	2.69	2.28	1.15	1.71	0.97	0.48	0.45	1.93	2.45	2.62	2.20	2.02	1.98	2.03	2.00	1.95	1.97	2.00	1.99	1.94
Fe^{tot}	2.24	2.28	1.80	1.73	1.80	2.27	2.48	2.21	0.49	0.47	0.02	0.64	0.45	1.00	1.85	1.86	1.90	1.47	1.93	1.86	2.44	1.81	1.57
Mn	0.03	0.03	0.01	0.02	0.03	0.01	0.03	0.06	0.00	0.00	0.00	0.00	0.00	0.03	0.06	0.10	0.06	0.58	0.19	0.15	0.10	0.48	0.55
Mg	2.01	2.47	1.57	2.20	2.29	1.71	2.05	1.65	0.07	0.15	0.00	0.00	0.00	0.00	0.38	0.12	0.38	0.08	0.17	0.25	0.27	0.08	0.21
Ca	0.32	1.52	0.19	1.63	1.62	0.15	1.32	0.16	0.11	0.11	0.99	2.01	1.95	1.98	0.72	0.90	0.65	0.87	0.79	0.77	0.30	0.66	0.75
Na	1.80	0.70	1.83	0.63	0.64	1.89	1.17	1.77	0.94	0.84	0.00	0.00	0.01	0.00	0.00	0.00	0.00	0.00	0.00	0.00	0.01	0.01	0.00
K	0.00	0.05	0.01	0.06	0.07	0.01	0.09	0.00	0.00	0.00	0.00	0.00	0.00	0.00	0.00	0.00	0.00	0.00	0.01	0.00	0.00	0.00	0.00
XMg	0.47	0.52	0.46	0.56	0.56	0.43	0.45	0.42	0.12	0.25	-	-	-	-	0.17	0.06	0.16	0.04	0.08	0.11	0.10	0.03	0.09
nOx	23	23	23	23	23	23	23	23	6	6	8	13	13	13	12	12	12	12	12	12	12	12	12

Table 2. (continued)

	chl											phg												
	3.01b	3.01b	3.04b	3.12b	3.12b	3.12d	3.12d	3.12d	3.28a	4.28a	4.35c	3.01b	3.01b	3.04b	3.04b	3.12b	3.12b	3.12d	3.27a	3.28a	4.20a	4.20a	4.28a	4.28a	4.35c
Analysis	b108	c66	d25	c83	c108	ag1	ag6	ag44	ag301	w5	aa27	c8	c65	d70	d85	c78	c125	ag38	c182	ag311	b1	b6	w4	w38	aa50
SiO_2	29.10	26.56	26.56	26.92	24.94	26.97	26.17	29.10	26.56	26.56	26.92	49.93	47.34	48.25	48.31	47.81	48.35	48.76	49.20	47.64	56.09	56.79	48.20	51.16	48.42
TiO_2	0.03	0.05	0.02	0.03	0.03	0.02	0.03	0.03	0.05	0.02	0.03	0.50	0.56	0.34	0.21	0.55	0.42	0.28	0.30	0.40	0.01	0.00	0.70	0.08	0.31
Al_2O_3	17.77	20.96	20.62	17.10	20.39	19.63	19.02	17.77	20.96	20.62	17.10	30.80	33.60	30.47	25.61	34.12	31.30	28.75	29.55	29.68	21.61	20.34	27.21	25.10	27.97
FeO	23.18	20.57	22.59	28.42	29.86	24.26	26.00	23.18	20.57	22.59	28.42	1.62	1.46	4.66	5.96	1.27	1.26	2.32	2.80	2.91	2.86	2.78	5.58	5.10	4.33
MnO	0.27	0.11	0.13	0.64	0.83	0.44	0.57	0.27	0.11	0.13	0.64	0.00	0.01	0.00	0.05	0.03	0.01	0.11	0.06	0.08	0.11	0.04	0.01	0.04	0.01
MgO	17.03	18.01	17.58	13.69	10.43	17.31	15.51	17.03	18.01	17.58	13.69	2.44	1.45	2.14	3.23	1.47	2.18	2.70	2.39	2.06	5.15	5.78	2.61	3.20	2.37
CaO	0.08	0.00	0.01	0.01	0.08	0.10	0.05	0.08	0.00	0.01	0.01	0.02	0.00	0.06	0.03	0.01	0.00	0.13	0.03	0.00	0.03	0.09	0.03	0.13	0.00
Na_2O	0.02	0.00	0.00	0.02	0.01	0.04	0.03	0.02	0.00	0.00	0.02	0.97	1.26	0.78	0.39	1.49	1.13	0.55	0.83	0.81	0.05	0.05	0.50	0.13	0.85
K_2O	0.00	0.02	0.01	0.05	0.01	0.02	0.02	0.00	0.02	0.01	0.05	9.42	9.54	9.70	9.92	9.15	9.78	10.39	9.72	9.66	10.57	10.99	10.45	10.99	8.84
S	87.47	86.27	87.51	86.88	86.57	88.79	87.40	87.47	86.27	87.51	86.88	95.70	95.22	96.37	93.72	95.89	94.42	93.99	94.87	93.22	96.46	96.85	95.29	95.95	93.09
												Structural formula													
Si	2.82	2.82	2.98	2.94	3.02	2.77	2.76	2.92	2.74	2.79	2.79	3.29	3.14	3.22	3.35	3.14	3.24	3.31	3.30	3.26	3.69	3.73	3.29	3.45	3.32
Ti	0.00	0.00	0.00	0.00	0.00	0.00	0.00	0.00	0.00	0.00	0.00	0.02	0.03	0.02	0.01	0.03	0.02	0.01	0.02	0.02	0.00	0.00	0.04	0.00	0.02
Al	2.67	2.48	2.17	2.30	2.18	2.57	2.52	2.19	2.64	2.39	2.39	2.39	2.63	2.40	2.09	2.64	2.47	2.30	2.33	2.39	1.67	1.57	2.19	1.99	2.26
Fe^{tot}	2.89	2.15	2.11	2.08	2.01	1.79	1.96	2.58	2.75	2.10	2.32	0.09	0.08	0.26	0.35	0.07	0.07	0.13	0.16	0.17	0.16	0.15	0.32	0.29	0.25
Mn	0.07	0.00	0.03	0.02	0.02	0.01	0.01	0.06	0.08	0.04	0.05	0.00	0.00	0.00	0.00	0.00	0.00	0.01	0.00	0.00	0.01	0.00	0.00	0.00	0.00
Mg	1.37	2.48	2.64	2.55	2.64	2.80	2.72	2.22	1.71	2.67	2.46	0.24	0.14	0.21	0.33	0.14	0.22	0.27	0.24	0.21	0.50	0.56	0.27	0.32	0.24
Ca	0.01	0.00	0.00	0.01	0.01	0.00	0.00	0.00	0.01	0.01	0.01	0.00	0.00	0.00	0.00	0.00	0.00	0.01	0.00	0.00	0.00	0.01	0.00	0.01	0.00
Na	0.00	0.01	0.00	0.01	0.00	0.00	0.00	0.00	0.00	0.01	0.01	0.12	0.16	0.10	0.05	0.19	0.15	0.07	0.11	0.11	0.01	0.01	0.07	0.02	0.11
K	0.00	0.01	0.01	0.01	0.00	0.00	0.00	0.01	0.00	0.00	0.00	0.79	0.81	0.83	0.88	0.77	0.84	0.90	0.83	0.84	0.89	0.92	0.91	0.95	0.77
XMg	0.32	0.54	0.55	0.55	0.56	0.61	0.58	0.46	0.38	0.56	0.51	0.73	0.64	0.45	0.49	0.67	0.75	0.66	0.60	0.55	0.76	0.78	0.45	0.53	0.49
nOx	14	14	14	14	14	14	14	14	14	14	14	11	11	11	11	11	11	11	11	11	11	11	11	11	11

[a]Mineral abbreviations are amp, amphibole; chl, chlorite; cpx, clinopyroxene; ep, epidote; g, garnet; lws, lawsonite; phg, phengite; nOx, number of oxygens used for the calculation of the structural formula.

Table 3. Example of Calculations Performed With THERMOCALC[a]

	Minerals Involved in the Paragenesis							P-T Calculations						
Sample	Am	Chl	Gt	Phg	Ep	Others	Mod[b]	P	dP	T	dT	cor	Fit	Fit[c]
3.01b														
Core	-	b108	c46	c8	-	ab, rt, sph	cl	10	1.1	523	12	0.03	0.1	1.7
Core	-	"	"	"	-	ab, rt, sph	am	12	1.7	529	16	−0.06	1.3	1.7
Rim	-	c66	c43	c65	-	ab	cl	9.2	1.4	570	15	0.06	1	1.7
3.04b														
	d62	d25	-	d85	d45		am	9.5	2.7	483	35	0.35	1.8	1.7
	d124	d58	-	d70	d48	ab	am	6.9	1.3	479	43	0.67	1.4	1.7
3.12b														
core	-	c108	c75	c78	c88	ab	am	12	0.9	565	17	0.56	1	
rim	-	c83	c120	c125	-	ab, rt, sph	am	10	1	515	18	0.61	1.3	
3.12d														
core	ag12	-	ag28	-	-	bi	tr	6.9	1.7	501	46	0.73	1.2	1, 61
rim	ag11	ag44	ag51	ag38	-	ab, rt, sph	am	10	0.9	539	16	0.24	1.1	
3.27a														
	-	c225	c238	c182	-	ab, rt sph	gr, am	13	1.5	579	15	0.02	1.1	
3.28a														
	-	ag301	ag294	ag311	-	ab, rt sph	am	12	0.9	518	12	0.32	1.1	1.6
4.28a														
NaCa amp	w69	w5	-	w38	w34		am, tr	11	1.6	471	22	0.38	1	
gln-post	w10	w14	-	w4	w34	ab, rt, sph		6.3	1	440	40	0.65	1.1	
4.35c														
	aa109	aa27	w95	aa50	aa98	ab		9.7	1	548	18	0.42	1.3	1.6
4.37b														
Pre	e162	-	e143	-	-	ab, bi		7.4	1.6	476	44	0.84	0.9	1.6
Post	e208	e177	e146	e198	-	ab		11	0.9	532	14	0.40	1.1	1.6

[a]THERMOCALC (version 3.2.1 [*Holland and Powell*, 1990, 1998]). The analyses quoted here can be found in Table 2. Mineral abbreviations are the same as for Table 2.

[b]End-members present only in small amounts (resulting in a large uncertainty in the results) that were removed in the calculations (am, amesite; cl, clinochlore; gr, grossular; tr, tremolite).

[c]Fit corresponds to a threshold value: results of the calculations (column fit) should be lower than this value to ensure reliability (see *Holland and Powell* [1998] for further details).

and others [e.g., *Anczkiewicz et al.*, 2000; *Glodny et al.*, 2005]. The Hajiabad BS were thus likely underplated in the hanging wall of the subduction zone (i.e., below the SSZ) and later juxtaposed to the feebly metamorphosed oceanic material of the colored melange (Figure 2d), possibly the last material accreted before the end of subduction. The systematic association of Hajiabad BS with serpentinites suggests that they facilitated the exhumation of the HP-LT rocks, as recognized in other natural settings [*Schwartz et al.*, 2000; *Guillot et al.*, 2001; *Schneider et al.*, 2004] and tested in thermomechanical modeling [*Gerya et al.*, 2002].

[57] Most importantly, our age results (Figure 9c) suggest that the exhumation of BS was transient with respect to the long-lived Neotethyan subduction (circa 150–35 Ma [*Berberian and King*, 1981; *McCall*, 1997]) and broadly coincide with large-scale obduction processes starting at circa 95 Ma from Cyprus to Oman [*Ricou*, 1971, 1994; *Hacker*, 1994]. Four major questions arise: (1) What is the relationship between Zagros and Oman BS? (2) Why do the BS sampled back at surface only span the period 95–85 Ma (and, to a lesser extent, 115–85 Ma)? (3) Why are there no BS exhumed after 80 Ma? (4) Why were blueschists only brought back to the surface in the southeasternmost corner of the Zagros?

6.2. What Is the Relationship Between Zagros BS and Oman HP-LT Rocks?

[58] In order to answer question 1, it is necessary to compare our age results for Zagros BS to age constraints for obduction and HP-LT metamorphism in Oman, which

Figure 9. (a) Example of in situ ^{40}Ar-^{39}Ar laser probe ablation. Overlays show surface areas from which argon was extracted. Numbers correspond to ages obtained. Phengite grains from the schistosity (black overlays) yield ages between 96 and 88 Ma, while younger ages on average (circa 91–84 Ma; white overlays) are encountered along late shear bands. Old ages (circa 91–90 Ma) along the shear bands could result from excess argon, as chlorite is present in minor amounts, or to imperfect recrystallization. (b) Radiometric ages obtained for all samples (also shown in Figure 2a). See Table 4 for detailed isotopic results. (c) Histogram of the radiometric ages obtained in this study (Figure 9b and Table 4) versus time. Dark bars indicate ages from Ashin + Sheikh Ali (asterisks, all samples from Ashin plus sample 3.28 from Sheikh Ali). White bars indicate data for all samples. Note that no ages younger than 80 Ma were obtained. SEZ, SE Zagros. (d) Histogram of radiometric ages versus time for Oman blueschists and eclogites. Data are from the literature [*Montigny et al.*, 1988; *El Shazly and Lanphere*, 1992; *Searle et al.*, 1994; *Saddiqi et al.*, 1995; *Poupeau et al.*, 1998; *El Shazly et al.*, 2001; *Warren et al.*, 2003, 2005; *Gray et al.*, 2004]. Dotted dark gray bars indicate Rb/Sr and U/Pb data; white bars indicate Ar-Ar data; gray bars indicate Ar-Ar plateau ages only; dashed bars indicate fission tracks in zircon (FT/Zr). Other major geological constraints are recalled: (1) inception of obduction movements through radiometric dating of metamorphic soles; (2) age of the youngest sediments overthrust by the ophiolite obduction nappe; and (3) age of the oldest sediments sealing the obduction thrust contacts.

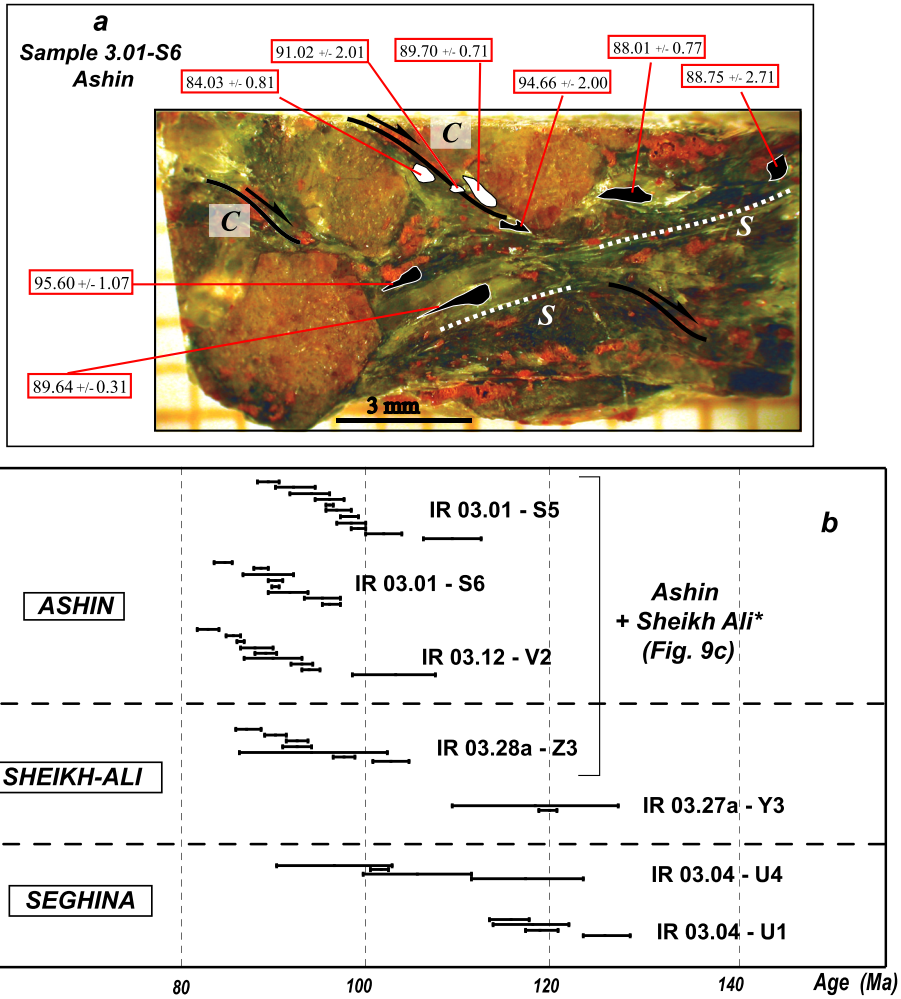
a
Sample 3.01-S6
Ashin
91.02 +/- 2.01
89.70 +/- 0.71
88.01 +/- 0.77
84.03 +/- 0.81
94.66 +/- 2.00
88.75 +/- 2.71
C
C
S
S
95.60 +/- 1.07
89.64 +/- 0.31
3 mm
b
IR 03.01 - S5
IR 03.01 - S6
IR 03.12 - V2
ASHIN
Ashin
+ Sheikh Ali*
(Fig. 9c)
IR 03.28a - Z3
SHEIKH-ALI
IR 03.27a - Y3
IR 03.04 - U4
SEGHINA
IR 03.04 - U1
80
100
120
140
Age (Ma)
Ashin + Sheikh Ali*
c
age constraints
SE Zagros (this study)
all SEZ
Number of ages
Age (Ma)
Rb/Sr + U/Pb
Ar (plateau only)
FT (Zr)
d
age constraints
Oman
all Ar
sediments sealing
the obduction stack
+
resumption
of extension
youngest sediments
below the obduction
nappe
beginning of intra-oceanic
obduction movements
continental subduction of the Arabian margin
HP-LT metamorphism (?)

Figure 9

Table 4. Results of Ar-Ar Radiometric Data[a]

Run	40*/39	36/40	39/40	37/39	% Atm	Age, Myr	1σ
				Ashin			
a	4.58	0.28	0.20	0.03	8.20	92.17	2.07
b	4.43	0.33	0.20	0.03	9.70	89.23	1.21
c	4.67	0.46	0.19	0.67	13.50	93.81	2.06
d	4.82	0.18	0.20	0.18	5.40	96.75	1.40
e	4.77	0.06	0.21	0.00	1.70	95.89	1.67
f	4.89	0.03	0.20	0.02	0.80	98.12	0.88
g	5.46	0.05	0.18	0.00	1.30	109.27	3.20
h	5.08	0.04	0.19	0.00	1.00	101.77	1.94
i	4.78	0.00	0.21	0.00	0.10	95.97	0.42
j	4.93	0.02	0.20	0.00	0.50	98.99	0.71
k	4.90	0.10	0.20	0.02	3.00	98.36	1.52
						97.3[b]	5.2[c]
b	4.53	0.33	0.20	0.03	9.70	91.02	2.01
c	4.17	0.36	0.21	0.16	10.70	84.03	0.81
d	4.46	0.20	0.21	0.00	5.90	89.70	0.71
e	4.76	0.29	0.19	0.05	8.50	95.60	1.07
f	4.37	0.34	0.21	0.03	10.00	88.01	0.77
g	4.41	0.32	0.20	0.00	9.50	88.75	2.71
h	4.46	0.33	0.20	0.07	9.60	89.64	0.31
j	4.71	0.27	0.20	0.24	7.90	94.66	2.00
						90.2	*3.7*
a	5.10	0.15	0.19	0.35	4.30	102.26	4.38
b	4.44	0.25	0.21	0.00	7.30	89.24	3.01
c	4.60	0.24	0.20	0.30	7.10	92.39	1.11
d	4.34	0.35	0.21	0.09	10.30	87.39	1.74
e	4.64	0.03	0.21	0.05	0.90	93.22	0.98
f	4.40	0.19	0.21	0.44	5.60	88.54	1.17
g	4.22	0.43	0.21	0.82	12.60	85.02	0.83
h	4.27	0.42	0.20	1.59	12.50	85.93	0.39
i	4.09	0.67	0.20	0.23	19.80	82.38	1.21
						89.6[b]	5.9[c]
				Sheikh Ali			
a	5.92	0.02	0.17	0.00	0.66	118.09	0.89
b	5.84	0.25	0.16	0.00	7.28	116.57	8.93
						117.3[b]	-
a	4.69	0.60	0.18	0.09	17.50	94.29	7.93
b	4.61	0.66	0.17	0.03	19.30	92.74	1.11
d	4.61	0.74	0.17	0.07	21.90	92.72	1.39
e	5.12	0.56	0.16	0.00	16.50	102.66	2.00
f	4.49	0.55	0.19	0.01	16.10	90.28	1.17
g	4.87	0.65	0.17	0.02	19.20	97.69	0.99
h	4.35	0.59	0.19	0.03	17.40	87.48	1.18
						94.0[b]	5.0[c]
				Seghina			
a	5.82	0.33	0.16	1.50	9.70	116.22	2.18
c	5.94	0.86	0.13	7.71	25.40	118.49	4.05
d	6.35	0.75	0.12	4.69	22.00	126.51	2.56
b	5.99	0.50	0.14	1.73	14.90	119.55	1.88
a	5.02	0.53	0.17	0.90	15.80	100.75	0.93
c	5.23	1.09	0.13	3.62	32.30	104.85	5.98
e	4.77	0.64	0.17	0.37	18.90	95.81	6.41
f	5.86	0.50	0.15	2.46	14.60	116.91	6.21
						112.4[b]	10.6[c]

[a]Isotopic ratios and associated errors are presented together with the amount of atmospheric argon (% atm).
[b]Average age value for the sample.
[c]Standard deviation.

include (1) inception of the Semail ophiolite thrust at 97–90 Ma by dating of the metamorphic sole [*Lanphere*, 1981; *Hacker*, 1994; *Hacker and Mosenfelder*, 1996], (2) deposition of the youngest, somewhat diachronous sediments deformed and metamorphosed below the ophiolite sole at circa 90–85 Ma [*Robertson*, 1987], (3) deposition of the oldest unconformable sediments on top of the ophiolite nappe pile by 70–65 Ma [*Glennie et al.*, 1990; *Breton et al.*, 2004; *Searle et al.*, 2004], and (4) radiometric age constraints for Oman BS and eclogites (Figure 9d; references in caption). The paleogeographic settings at present and at the onset of this large-scale obduction (displacement ~400 km [*Searle et al.*, 2004]) are compared on Figures 10a and 10b.

[59] A detailed discussion of radiometric ages is beyond the scope of the present paper: age data for Oman are even more scattered than for Zagros and the possibility of two HP-LT events is debated [e.g., *Gray et al.*, 2004; *Warren et al.*, 2005]. Considering the compilation of Figure 9d and the other available time constraints, a reasonable interpretation, however, is to consider that Rb/Sr and U/Pb ages yield the HP-LT event at around 80–78 Ma (as argued by *Searle and Cox* [1999] and *Warren et al.* [2005]) and that excess argon contaminated most of Ar ages. HP-LT metamorphism in the SE Zagros, assuming only a minor excess argon bias, may have therefore predated by ~5–10 Myr that of the Oman continental margin (Figures 9c and 9d).

[60] We so far implicitly assumed that the Zagros BS had formed in the subduction zone beneath Iran, north of the intraoceanic obduction thrust (hypothesis 1). An alternative tectonic explanation, placing them to the south (hypothesis 2; Figure 10c), is discussed in the following because it might be argued that (1) HP-LT rocks from Oman and SE Zagros do not lie on the same SW-NE transect (Figures 1a and 10a) and (2) if excess argon in Zagros BS is as important as in Oman BS, radiometric ages might be roughly similar for Zagros and Oman (Figures 9c and 9d). Zagros BS could then be regarded as Oman BS equivalents (i.e., formed below the obduction nappe) and this would explain why Zagros BS of roughly the same age as Oman BS crop out near the Oman-Zagros-Makran junction (question 4).

[61] Several arguments, however, support hypothesis 1 (Figure 10c):

[62] 1. Zagros BS are found among truly oceanic units and are closely associated with serpentinites. Oman BS, on the contrary, correspond to Paleozoic to Cretaceous continental rocks from the Arabian platform [*Gray et al.*, 2004; *Searle et al.*, 2004]. No oceanic rocks occur below the obducted nappe in Oman.

[63] 2. Zagros BS lithologies (and the lack of metapelites) suggest that the material entering the subduction wedge was dominated by volcanoclastics derived from an active margin (Iran) rather than from a platform (Arabia). The same holds true for the fact that some of Ashin rocks resemble lower Cretaceous series from the SSZ and that the first equilibration steps along the P-T-t paths might represent an earlier metamorphic imprint (Figure 8a).

[64] 3. Higher-pressure, eclogitic conditions around 23 kbar/550°C were reported for Oman [e.g., *Searle et al.*, 1994] than for Zagros (17–18 kbar, this study).

[65] 4. Exhumation-related deformation patterns are very different in the Zagros and in Oman. Synorogenic E-W, orogen-parallel, relatively coaxial stretching prevailed during exhumation in SE Zagros (Figure 4), whereas exhumation patterns in Oman are marked by extensional, noncoaxial NE vergent movements at right angles with the trend of the orogen, and were followed by brittle extension [*Jolivet et al.*, 1998]. These latter characteristics

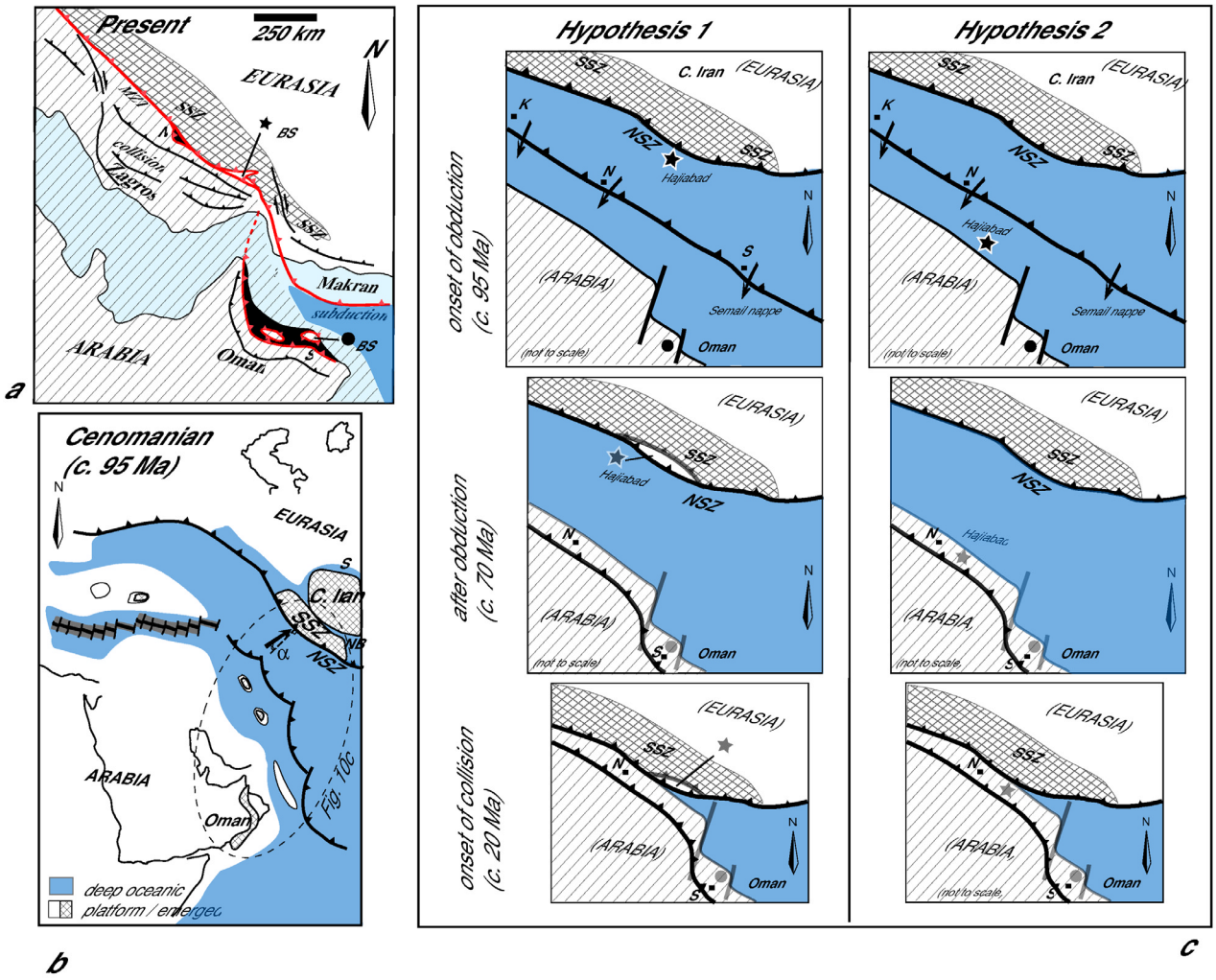

Figure 10. (a) Present-day tectonic map across Hormoz strait showing the boundaries between Arabia and Eurasia. (b) Paleogeodynamic situation of the Neotethyan realm between Arabia and Eurasia at the onset of obduction (modified after *Sengör et al.* [1988], *McCall* [1997], *Dercourt et al.* [2000], and *Stampfli and Borel* [2002]). The Neotethyan subduction zone (NSZ) beneath Iran (i.e., central Iran plus the Sanandaj-Sirjan zone; SSZ) and the large-scale intraoceanic obduction thrust are shown. Small, discontinuous oceanic domains formed slightly later, during the period 83–60 Ma (NB, Nain-Baft; S, Sabzevar), are also indicated. (c) Simple paleogeographic maps drawn at circa 95, 70, and 20 Ma in order to compare two different hypotheses. Hypothesis 1 shows that Zagros BS are formed in the subduction zone beneath Iran. Hypothesis 2 shows that Zagros BS are formed, like Oman BS and eclogites, below the obduction nappe. The two sets of maps are to be compared with the sketch map of Figure 10a. Obducted ophiolites: K, Kermanshah; N, Neyriz; S, Semail.

are diagnostic of postorogenic exhumation [*Jolivet et al.*, 2004].

[66] 5. To the SW, Zagros BS are underlain by an Eo-Oligocene flysch unit with oceanic olistoliths. In hypothesis 2, this flysch would be expected to lie on the NE side of Zagros BS.

[67] 6. The Neyriz obducted ophiolite lies below the MZT, whereas the Zagros BS lie above. The opposite would be expected from hypothesis 2 (Figure 10c).

6.3. A Model for the Exhumation of Zagros BS

[68] On the basis of radiometric age constraints for Zagros BS (circa 115–85 Ma; Figures 9b and 9c) and on the existence of obduction movements in the region during the period 95–70 Ma, we propose that Zagros BS were transiently exhumed in the NSZ subduction zone due to a modification of the mechanical coupling between the upper and lower plate in response to obduction processes (Figure 11a). This exhumation process was short-lived and stopped at around 80 Ma, that is when the Arabian continental margin entered the subduction zone in the southern Neotethyan realm. From then onward, exhumation appears to have been inhibited along the northern Neotethyan convergent boundary and HP-LT rocks irreversibly dragged to depths, as for other convergent settings devoid of BS (e.g., the Andes [*Maruyama et al.*, 1996; *Jaillard et al.*,

2002, and references therein]). Makran blueschists dated at 87.9 ± 5.5 Ma [*Delaloye and Desmons*, 1980] (Figure 1b) could represent further evidence of this transient, Late Cretaceous exhumation. Regional-scale extension immediately following obduction in Oman [*Mann et al.*, 1990; *Michard et al.*, 1994; *Jolivet et al.*, 1998] could, at least hypothetically, testify to the resumption of slab-pull forces along the subduction zone beneath Iran (Figure 11a, step 4).

[69] In order to further test this hypothesis, simple kinematic calculations were performed to constrain convergent processes across the NSZ. The following assumptions were made to evaluate the respective movement between Arabia and the SSZ (Figure 11b): (1) the SSZ is attached to Eurasia during the period 145 to 65 Ma, (2) the NSZ strikes NW-SE (i.e., following the edge of the SSZ), (3) the northern edge of Arabia is now located some 50–70 km north of the MZT (points 1–3, Figure 11b, right) due to collisional shortening [*Molinaro et al.*, 2005], and (4) kinematic paths for points 1–3 were calculated using the Eurasia/Arabia rotation pole data of *Müller et al.* [1997] and the algorithms of *Cox and Hart* [1986].

[70] Assumption 1 is known to be somewhat erroneous due to the existence of two additional, short-lived oceanic domains between Arabia and Eurasia (now represented by the discontinuous Nain-Baft and Sabzevar ophiolites; Figures 1a and 10b). However, both the back-arc Nain-Baft oceanic domain and the Sabzevar oceanic domain are thought to have opened during the Campanian and closed in the Paleocene (circa 83–60 Ma [*Davoudzadeh*, 1972; *Baroz et al.*, 1984; *Sengör et al.*, 1988; *Arvin and Robinson*, 1994; *Stampfli and Borel*, 2002; *Shojaat et al.*, 2003]) as a result of wrench movements accompanying the anticlockwise rotation of the Lut block [*Soffel and Förster*, 1984; *Sengör*, 1990]. They represented narrow seaways with discontinuous oceanic crust emplacement [e.g., *Baroz et al.*, 1984; *Arvin and Robinson*, 1994]. Estimates of SSZ/Arabia convergence velocities inferred from Eurasia/Arabia movements will therefore be wrong to some extent, but the misfit should not be very large. Large-scale rotations of the SSZ, on the other hand, can be ruled out since the Mesozoic Magmatic belt in the SSZ (Figure 1a) is parallel to both the suture zone (along the MZT) and to the Tertiary Urumieh-Dokhtar magmatic arc.

[71] The results show (Figures 11c and 11d): (1) a sharp increase of velocities, which more than doubled and reached 5–6 cm yr^{-1}, during the period 118–85 Ma, before the opening of the Nain-Baft and Sabzevar oceanic domains (Figure 11d); (2) a marked change in convergence directions at 118 Ma ($\sim$20°, Figure 11d) followed by a more-or-less continuous decrease of the convergence obliquity across the northern Neotethyan convergent zone; (3) a velocity decrease, in several steps from 85 to 70 Ma, whereby velocities were stabilized at $\sim$3–3.5 cm yr^{-1} toward the end of the Cretaceous (this latter value is in agreement with recent estimates of kinematic velocities across this area for the Early Tertiary ($\sim$3.2 cm yr^{-1}) [*McQuarrie et al.*, 2003]); and (4) a slight increase of the velocities (15–20%) from north to south (points 1–3). Although these kinematic calculations are fraught with uncertainties regarding the Eurasia/SSZ movements, they reveal a striking coincidence between the high-velocity/low obliquity 118–85 Ma period and the radiometric ages obtained for the SE Zagros BS (Figure 11d).

[72] We therefore tentatively propose that high convergence velocities and/or the amount of shortening absorbed by obduction to the south (which created a new convergent system along the north of Arabia) affected the mechanical coupling between the upper and lower plate in the northern subduction zone beneath Iran, and allowed for the transient exhumation of the Zagros BS (between 95–85 and, to a lesser extent, 115–85 Ma) to shallower depths (<15–20 km at 80 Ma). High convergence velocities (and low obliquity) during the period 118-85 Ma would have favored the formation of BS along the NSZ (Figure 11a) as a result of (1) the existence of a cooler P-T gradient in the subduction wedge leading to the formation of true BS (rather than epidote amphibolites, which should perhaps be looked for along the MZT) and (2) increased circulation of HP-LT material in the subduction wedge [*Cloos*, 1982].

6.4. Why Are BS Only Found in the SE Corner of Zagros?

[73] This geotectonic scenario (Figure 10c, hypothesis 1; Figure 11a) provides answers to questions 1–3 above. It does not explain why BS are only found in the SE corner of Zagros (question 4). To account for this observation, two contrasted interpretations can be envisaged: either BS exhumation processes were efficient enough only in the SE of Zagros, or BS exhumation took place all along the Zagros but to intermediate depths only, surface exposures being restricted to the area around Hajiabad.

[74] In support of the first interpretation, it can be argued that the obduction process may not have been cylindrical (i.e., the Omanese margin was buried deeper than the Arabian platform further north [*Breton et al.*, 2004]) and that convergence velocities in the north were lower than in the south by 15–20%. Several lines of evidence support the

Figure 11. (a) Interpretative sketches relating the formation and exhumation of Zagros BS during the period 115–80 Ma (95–85 Ma, mainly) to obduction movements and increased convergence velocities (see Figures 11b–11d). See text for details. (b) Paleogeodynamic map of the Neotethyan realm at the onset of obduction (see Figure 10b) showing the location of points 1–3, for which paleopositions during the period 145 to 65 Ma were calculated (Figures 11c–11d). The respective positions of the three main ophiolite relics obducted during the Upper Cretaceous (i.e., Kermanshah, Neyriz, Semail) are indicated. (c) Estimates of the paleopositions of points 1–3 (Figure 11b) during the period 145 to 65 Ma, assuming that these points marked the northern edge of Arabia. See section 6.3 for details. (d) Evolution of Arabia/SSZ convergence velocities (in cm yr^{-1}) and obliquity as a function of time for points 1 to 3 (from NW to SE) located in Figure 11b. Obliquity refers here to the angle (α; Figure 10b) between the convergence direction and the direction at right angles with the subduction margin ($\alpha > 0$ when the strike of the convergence direction more than to N045°E). The strike of the northern Neotethyan subduction zone during that period is taken as NW-SE (i.e., along the SSZ in Figure 10b). Note that the period 115–85 Ma of high velocities (i.e., >5 cm yr^{-1} for SE Zagros) coincides with the ages of exhumed blueschists (Figures 9b and 9c).

second interpretation. First, the Hajiabad BS crop out in a part of the Zagros showing strong singularities, both in terms of topography and seismicity (Figure 1a, inset). The region appears to have been more strongly uplifted than adjacent parts of Zagros along strike and this is consistent with the cross section of Figure 2d. This is also the only place along the Zagros where deep earthquakes (>30 km; Figure 1a) occur to the north of the MZT. Second, the final

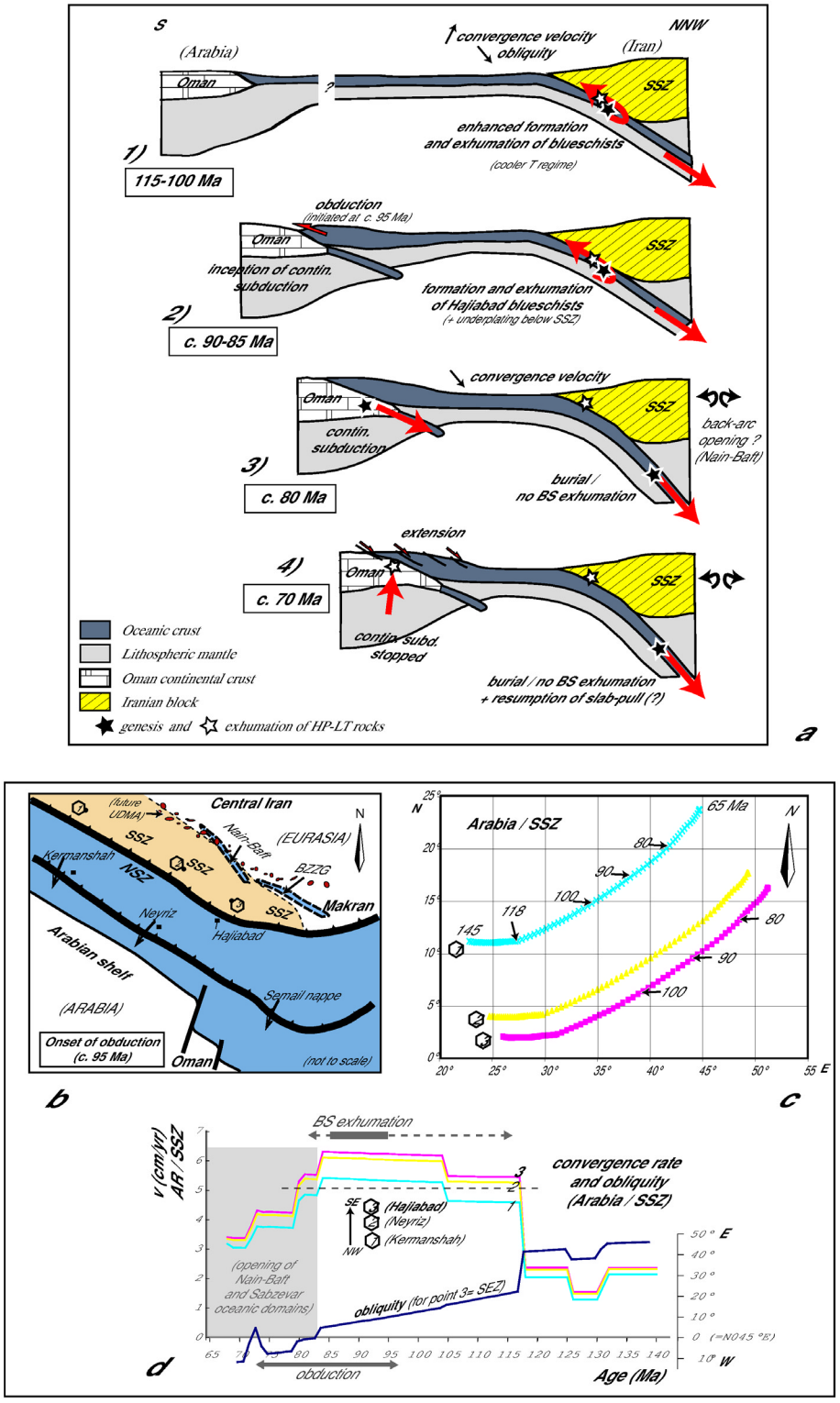

Figure 11

exhumation of BS could have been locally enhanced by a more complex three-dimensional geometry at depths due to inherited tectonic patterns (e.g., Oman line), or to the transition between collision and subduction. Its location bears resemblances with the Himalayan syntaxes and their exhumation patterns [e.g., *Ding et al.*, 2001; *Zeitler et al.*, 2001]. For these reasons, we tend to favor the second interpretation, but the two hypotheses are not mutually incompatible.

7. Conclusions

[75] The main results of our study can be summarized as follows:

7.1. Structure

[76] Zagros BS are located just at the rear of the Main Zagros Thrust, in a very peculiar location near the transition between collision (Zagros) and subduction (Makran). They crop out in a general antiformal structure within the regional colored melange marking discontinuously the Zagros suture zone, in a window below the Sanandaj-Sirjan zone (SSZ). These BS crop out as coherent kilometer-scale bodies (one exception are the BS meter-sized blocks of Seghina encased in matrix serpentinite) associated with serpentinites which likely promoted their exhumation. Deformation of the blueschists is dominated by flattening and accompanied by subsequent greenschist facies stretching directions striking E-W on average.

7.2. P-T Conditions of HP-LT Metamorphism

[77] P-T estimates using THERMOCALC, TWEEQU, and Raman spectroscopy of carbonaceous material, point to HP-LT conditions for Gt-Phg-Chl-Rt ± Amph ± Ep ± Ti ± Bt assemblages around 11 kbar and 520–530°C on average, that is along a ~15°C km^{-1}, relatively warm subduction zone gradient. Before the onset of BS facies metamorphism, some of these rocks equilibrated at conditions around 7 kbar and 470 °C (samples 3.12d and 4.37b). Lawsonite-omphacite-bearing BS from Seghina unit point to higher-P conditions, around 17–18 kbar and 500°C. Exhumation P-T paths testify to relatively cold return conditions.

7.3. Age and Genetic Geodynamic Context of the Blueschists

[78] SE Zagros BS represent intermediate to mafic protoliths buried to depths of 35–50 km. In situ, laser probe ^{40}Ar-^{39}Ar radiometric age constraints on phengite yield cooling ages between 95 and 85 Ma, with a scatter of up to 115 Ma. These ages coincide with the initiation of obduction movements in the region (circa 95 Ma) and are shown to be 5–10 Myr older than ages for the nearby Oman HP-LT rocks. Exhumation to midcrustal depths <15–20 km was accomplished before 80 Ma at rates on the order of 1–2 mm yr^{-1}. On structural, metamorphic and radiometric grounds, we conclude that Zagros BS were exhumed in the Neotethyan subduction zone beneath Iran (NSZ) during a transient period (circa 95–85 Ma mainly) with respect to long-lived subduction processes (circa 150–35 Ma). Convergence velocity estimates based on the Eurasia/Arabia kinematics reveal that this transient exhumation also coincided with a period of high convergence velocities (circa 118–85 Ma; Figure 11d).

7.4. Regional-Scale Implications and Interpretation

[79] We propose that the exhumation of Zagros BS corresponded to a transient process (circa 95–85 Ma, and to a lesser extent 115–85 Ma) during which the mechanical coupling and the subduction regime of the NSZ were temporarily modified by obduction processes on the Arabian margin and/or high convergence velocities. Exhumation stopped when the continental subduction of the northern edge of Arabia (Oman) and obduction ceased (circa 80–75 Ma). From then onward, BS would have been irreversibly subducted. As discussed in the text, the final exhumation of BS in the SE corner of Zagros probably results from a combination of local structural and topographic controls.

[80] **Acknowledgments.** We are most thankful to the Geological Survey of Iran for the logical support in the field. This work benefited from the financial support of the Middle East Basin Program (MEBE) and from additional funding from CNRS-Dyeti. This paper greatly benefited from the comments of W. G. Ernst, A. Okay, and J. Spray. Thanks are due to O. Beyssac and B. Goffé (Laboratoire de Géologie, ENS Paris) for providing access to their Raman spectroscopy facilities and for careful checks on samples 4.36a and 4.36b.

References

Agard, P., L. Jolivet, and B. Goffé (2001), Tectonometamorphic evolution of the Schistes Lustrés complex: Implications for the exhumation of HP and UHP rocks in the western Alps, *Bull. Soc. Geol. Fr.*, *172*, 617–636.

Agard, P., P. Monié, L. Jolivet, and B. Goffé (2002), In situ laser probe ^{40}Ar/^{39}Ar dating of the Schistes Lustrés complex: Implications for the exhumation of the western Alps, *J. Metamorph. Geol.*, *20*, 599–618.

Agard, P., L. Labrousse, S. Elvevold, and C. Lepvrier (2005a), Discovery of Palaeozoic Fe-Mg carpholite (Motalafjella, Svalbard Caledonides): A milestone for subduction zone gradients, *Geology*, *33*, 761–764.

Agard, P., J. Omrani, L. Jolivet, and F. Mouthereau (2005b), Convergence history across Zagros (Iran): Constraints from collisional and earlier deformation, *Int. J. Earth Sci.*, *94*, 401–419.

Alavi, M. (1994), Tectonics of the Zagros orogenic belt of Iran: New data and interpretations, *Tectonophysics*, *229*, 211–238.

Allen, M., J. Jackson, and R. Walker (2004), Late Cenozoic reorganization of the Arabia-Eurasia collision and the comparison of short-term and long-term deformation rates, *Tectonics*, *23*, TC2008, doi:10.1029/2003TC001530.

Anczkiewicz, R., J. P. Burg, I. M. Villa, and M. Meier (2000), Late Cretaceous blueschist metamorphism in the Indus Suture Zone, Shangla region, Pakistan Himalaya, *Tectonophysics*, *324*, 111–134.

Arnaud, N. O., and S. P. Kelley (1995), Evidence for excess argon during high pressure metamorphism in the Dora Maira Massif (western Alps, Italy), using an ultra-violet laser ablation microprobe ^{40}Ar-^{39}Ar technique, *Contrib. Mineral. Petrol.*, *121*, 1–11.

Arvin, M., and P. T. Robinson (1994), The petrogenesis and tectonic setting of lavas from the Baft ophiolitic melange, southwest of Kerman, Iran, *Can. J. Earth Sci.*, *31*, 824–834.

Augier, R., P. Agard, P. Monié, L. Jolivet, C. Robin, and G. Booth-Rea (2005), Exhumation, doming and slab retreat in the Betic Cordillera (SE Spain): In situ ^{40}Ar/^{39}Ar ages and P-T-d-t paths for the Nevado-Filabride complex, *J. Metamorph. Geol.*, *23*, 357–381.

Baroz, F., J. Macaudière, R. Montigny, M. Noghreyan, M. Ohnenstetter, and G. Rocci (1984), Ophiolites and related formations in the central part of the Sabzevar range (Iran) and possible geotectonic reconstructions, *Neues Jahrb. Geol. Palaeontol. Abh.*, *168*, 358–388.

Bebout, G. E. (1996), Volatile transfer and recycling at convergent margins: Mass-balance and insights from high-P/T metamorphic rocks, in *Subduction: Top to Bottom*, *Geophys. Monogr. Ser.*, vol. 96, edited by G. E. Bebout et al., pp. 179–193, AGU, Washington, D. C.

Berberian, M., and G. C. P. King (1981), Towards a paleogeography and tectonic evolution of Iran, *Can. J. Earth Sci.*, *18*, 210–265.

Berman, R. G. (1991), Thermobarometry using multi-equilibrium calculations: A new technique, with petrological applications, *Can. Mineral.*, *29*, 833–855.

Beyssac, O., B. Goffé, C. Chopin, and J. N. Rouzaud (2002), Raman spectra of carbonaceous material in metasediments: A new geothermometer, *J. Metamorph. Geol.*, *20*, 859–871.

Beyssac, O., B. Goffé, J. P. Petitet, E. Froigneux, M. Moreau, and J. N. Rouzaud (2003), On the characterization of disordered and heterogeneous carbonaceous materials using Raman spectroscopy, *Spectrochim. Acta*, *59*, 2267–2276.

Beyssac, O., L. Bollinger, J. P. Avouac, and B. Goffé (2004), Thermal metamorphism in the lesser Himalaya of Nepal determined from Raman spectroscopy of carbonaceous material, *Earth Planet. Sci. Lett.*, *225*, 233–241.

Braud, J. (1987), La suture du Zagros au niveau de Kermanshah (Kurdistan iranien): Reconstitution paléogéographique, évolution géodynamique, magmatique et structurale, 450 pp., Univ. Paris-Sud, Orsay, France.

Breton, J. P., F. Béchennec, J. Le Métour, L. Moen-Maurel, and P. Razin (2004), Eoalpine (Cretaceous) evolution of the Oman Tethyan continental margin: Insights from a structural field study in Jabal Akhdar (Oman mountains), *GeoArabia*, *9*, 1–19.

Burov, E., L. Jolivet, L. Le Pourhiet, and A. Poliakov (2001), A thermomechanical model of exhumation of high pressure (HP) and ultra-high pressure (UHP) metamorphic rocks in Alpine-type collision belts, *Tectonophysics*, *342*, 113–136.

Chemenda, A. I., M. Mattauer, J. Malavieille, and A. N. Bokun (1995), A mechanism for syn-collisional rock exhumation and associated normal faulting: Results from physical modelling, *Earth Planet. Sci. Lett.*, *132*, 225–232.

Cloos, M. (1982), Flow melanges: Numerical modeling and geologic constraints on their origin in the Franciscan subduction complex, California, *Geol. Soc. Am. Bull.*, *93*, 330–345.

Cloos, M. (1985), Thermal evolution of convergent plate margins: Thermal modeling and re-evaluation of isotopic Ar-ages for blueschists in the Franciscan complex of California, *Tectonics*, *4*, 421–433.

Cox, A., and R. B. Hart (1986), *Plate Tectonics. How It Works*, 392 pp., Blackwell, Malden, Mass.

Davoudzadeh, M. (1972), Geology and petrography of the area north of Nain, central Iran, 89 pp., Geol. Surv. of Iran, Tehran.

Delaloye, M., and J. Desmons (1980), Ophiolites and melange terranes in Iran: A geochronological study and its paleotectonic implications, *Tectonophysics*, *68*, 83–111.

DeMets, C., R. G. Gordon, D. F. Argus, and S. Stein (1990), Current plate motion, *Geophys. J. Int.*, *101*, 425–478.

Dercourt, J., L. E. Ricou, and B. Vrielynck (1993), *Atlas Tethys Palaeoenvironmental Maps*, 14 maps, 1 plates, Gauthier-Villars, Paris.

Dercourt, J., M. Gaetani, B. Vrielynck, E. Barrier, B. Biju-Duval, M. F. Brunet, J. P. Cadet, S. Crasquin, and M. Sandulescu (2000), *Atlas Peri-Tethys, Palaeogeographical Maps*, 24 maps and explanatory notes, Comm. for the Geol. Map of the World, Paris.

Ding, L., D. Zhong, A. Yin, P. Kapp, and T. M. Harrison (2001), Cenozoic structural and metamorphic evolution of the eastern Himalayan syntaxis (Namche Barwa), *Earth Planet. Sci. Lett.*, *192*, 423–438.

El-Shazly, A. K., and M. A. Lanphere (1992), Two high pressure metamorphic events in NE Oman: Evidence from $^{40}Ar/^{39}Ar$ and petrological data, *J. Geol.*, *100*, 731–751.

El-Shazly, A. K., M. Bröcker, B. Hacker, and A. Calvert (2001), Formation and exhumation of blueschists and eclogites from NE Oman: New perspectives from Rb-Sr and $^{40}Ar/^{39}Ar$ dating, *J. Metamorph. Geol.*, *19*, 233–248.

Ernst, W. G. (1972), Occurrence and mineralogical evolution of blueschist-belts with time, *Am. J. Sci.*, *272*, 657–668.

Ernst, W. G. (1988), Tectonic history of subduction zones inferred from retrograde blueschist P-T paths, *Geology*, *16*, 1081–1084.

Evans, B. W. (1990), Phase relations of epidote-blueschists, *Lithos*, *25*, 3–23.

Fotoohi Rad, G. R., G. T. R. Droop, S. Amini, and M. Moazzen (2005), Eclogites and blueschists of the Sistan Suture Zone, eastern Iran: A comparison of P-T histories from a subduction melange, *Lithos*, *84*, 1–24.

Gansser, A. (1955), New aspects of the geology in central Iran, in *4th World Petroleum Congress Proceedings*, vol. I/A/5, pp. 279–300, C. Colombo, Rome.

Gerya, T. V., B. Stöckhert, and A. L. Perchuk (2002), Exhumation of high-pressure metamorphic rocks in a subduction channel: A numerical simulation, *Tectonics*, *21*(6), 1056, doi:10.1029/2002TC001406.

Ghasemi, H., T. Juteau, H. Bellon, M. Sabzehei, H. Whitechurch, and L. E. Ricou (2002), The mafic-ultramafic complex of Sikhoran (central Iran): A polygenetic ophiolite complex, *C. R. Acad.*, *334*, 431–438.

Ghazi, A. M., A. A. Hassanipak, J. J. Mahoney, and R. A. Duncan (2004), Geochemical characteristics, ^{40}Ar-^{39}Ar ages and original tectonic setting of the Band-e-Zeyarat/Dar Anar ophiolite, Makran accretionary prism, SE Iran, *Tectonophysics*, *393*, 175–196.

Giorgis, D., M. Cosca, and S. Li (2000), Distribution and significance of extraneous argon in UHP eclogite (Sulu terrain, China): Insights from in situ $^{40}Ar/^{39}Ar$ UV-laser ablation analysis, *Earth Planet. Sci. Lett.*, *181*, 605–615.

Glennie, K. W., M. W. Hughes-Clarke, M. G. A. Boeuf, W. F. H. Pilaar, and B. M. Reinhardt (1990), Inter-relationship of Makran-Oman mountains belts of convergence, in *The Geology and Tectonics of the Oman Region*, edited by A. H. F. Robertson, M. P. Searle, and A. C. Ries, *Geol. Soc. Spec. Publ.*, *49*, 773–786.

Glodny, J., J. Lohrmann, H. Echtler, K. Grafe, W. Seifert, S. Collao, and O. Figueroa (2005), Internal dynamics of a paleoaccretionary wedge: Insights from combined isotope tectonochronology and sandbox modelling of the south-central Chilean forearc, *Earth Planet.y Sci. Lett.*, *231*, 23–39.

Goffé, B., A. Michard, J. R. Kienast, and O. Le Mer (1988), A case of obduction-related high-pressure, low-temperature metamorphism in upper crustal nappes, Arabian continental margin, Oman: P-T paths and kinematic interpretation, *Tectonophysics*, *151*, 363–386.

Gray, G. R., M. Hand, J. Mawby, R. A. Armstrong, J. M. Miller, and R. T. Gregory (2004), Sm-Nd and Zircon U-Pb ages from garnet-bearing eclogites, NE Oman: Constraints on High-P metamorphism, *Earth Planet. Sci. Lett.*, *222*, 407–422.

Grove, M., and G. E. Bebout (1995), Cretaceous tectonic evolution of coastal southern California: Insights from the Catalina Schist, *Tectonics*, *14*, 1290–1308.

Guillot, S., K. H. Hattori, J. de Sigoyer, T. Nagler, and A.-L. Auzende (2001), Evidence of hydration of the mantle wedge and its role in the exhumation of eclogites, *Earth Planet. Sci. Lett.*, *193*, 115–127.

Hacker, B. R. (1994), Rapid emplacement of young oceanic lithosphere: Argon geochronology of the Oman ophiolite, *Science*, *265*, 1563–1565.

Hacker, B. R., and J. L. Mosenfelder (1996), Metamorphism and deformation along the emplacement thrust of the Samail ophiolite, Oman, *Earth Planet. Sci. Lett.*, *144*, 435–451.

Hatzfeld, D., M. Tatar, K. Priestley, and M. Ghafory-Ashtiany (2003), Seismological constraints on the crustal structure beneath the Zagros Mountain belt (Iran), *Geophys. J. Int.*, *155*, 403–410.

Hessami, K., H. A. Koyi, C. J. Talbot, H. Tabasi, and E. Shabanian (2001), Progressive unconformities within an evolving foreland fold-thrust belt, Zagros Mountains, *J. Geol. Soc. London*, *158*, 969–981.

Holland, T. J. B., and R. Powell (1990), An enlarged and updated internally consistent thermodynamic dataset with uncertainties and correlations: The system K_2O-Na_2O-CaO-MgO-MnO-FeO-Fe_2O_3-Al_2O_3-TiO_2-SiO_2-C-H_2-O_2, *J. Metamorph. Geol.*, *8*, 89–124.

Holland, T. J. B., and R. Powell (1998), An internally consistent thermodynamic data set for phases of petrological interest, *J. Metamorph. Geol.*, *16*, 309–343.

Hubbard, M. S., D. A. Spencer, and D. P. West (1995), Tectonic exhumation of the Nanga Parbat massif, northern Pakistan, *Earth Planet. Sci. Lett.*, *133*, 213–225.

Jackson, J., J. Hains, and W. Holt (1995), The accommodation of Arabia-Eurasia plate, *J. Geophys. Res.*, *100*, 15,205–15,219.

Jaillard, E., G. Hérail, T. Monfret, and G. Wörner (2002), Andean geodynamics: Main issues and contributions from the 4th ISAG, Göttingen, *Tectonophysics*, *345*, 1–15.

Jolivet, L., B. Goffé, R. Bousquet, R. Oberhänsli, and A. Michard (1998), Detachments in high-pressure mountain belts, Tethyan examples, *Earth Planet. Sci. Lett.*, *160*, 31–47.

Jolivet, L., C. Faccenna, B. Goffé, E. Burov, and P. Agard (2003), Subduction tectonics and exhumation of HP metamorphic rocks of the Mediterranean orogens, *Am. J. Sci.*, *303*, 353–409.

Jolivet, L., V. Famin, C. Mehl, T. Parra, C. Aubourg, R. Hebert, and P. Philippot (2004), Strain localization during crustal-scale boudinage to form extensional metamorphic domes in the Aegean Sea, in *Gneiss Domes in Orogeny*, edited by D. L. Whitney, C. Teyssier, and C. S. Siddoway, *Spec. Pap. Geol. Soc. Am.*, *380*, 185–210.

Jolivet, L., H. Raimbourg, L. Labrousse, D. Avigad, Y. Leroy, H. Austrheim, and T. B. Andersen (2005), Softening triggerred by eclogitization, the first step toward exhumation during continental subduction, *Earth Planet. Sci. Lett.*, *237*, 532–547.

Kretz, R. (1983), Symbols for rock-forming minerals, *Am. Mineral.*, *68*, 277–279.

Labrousse, L., L. Jolivet, T. B. Andersen, P. Agard, R. Hébert, H. Maluski, and U. Schärer (2004), Pressure-temperature–time-deformation history of the exhumation of ultra-high pressure rocks in the Western Gneiss region, Norway, in *Gneiss Domes in Orogeny*, edited by D. L. Whitney, C. Teyssier, and C. S. Siddoway, *Spec. Pap. Geol. Soc. Am.*, *380*, 155–183.

Lanphere, M. A. (1981), K-Ar ages of metamorphic rocks at the base of the Samail ophiolite, Oman, *J. Geophys. Res.*, *86*, 2777–2782.

Lanphere, M. A., and J. Pamic (1983), $^{40}Ar/^{39}Ar$ ages and tectonic setting of ophiolite from the Neyriz area, southeast Zagros range, Iran, *Tectonophysics*, *96*, 245–256.

Leake, B. E., et al. (1997), Nomenclature of amphiboles: Report of the Subcommittee on Amphiboles of the International Mineralogical Association Commission on new minerals and mineral names, *Eur. J. Mineral.*, *9*, 623–651.

Maluski, H., and P. Monié (1988), $^{40}Ar/^{39}Ar$ laser-probe multi-dating inside single biotites of a Variscan orthogneiss (Pinet Massif Central, France), *Chem. Geol.*, *73*, 245–263.

Mann, A., S. S. Hanna, and S. C. Nolan (1990), The post-Campanian tectonic evolution of the central Oman Mountains: Tertiary extension of the eastern Arabian margin, in *The Geology and Tectonics of the Oman Region*, edited by A. H. F. Robertson, M. P. Searle, and A. C. Ries, *Geol. Soc. Spec. Publ.*, *49*, 797–831.

Maruyama, S., J. G. Liou, and M. Terabayashi (1996), Blueschist and eclogites of the world and their exhumation, *Int. Geol. Rev.*, *38*, 485–594.

McCall, G. J. H. (1997), The geotectonic history of the Makran and adjacent areas of southern Iran, *J. Asian Earth Sci.*, *15*, 517–531.

McCall, G. J. H., and R. G. W. Kidd (1981), The Makran, southeastern Iran: The anatomy of a convergent plate margin active from Cretaceous to Present, in *Trench-Forearc Geology: Sedimentation and Tectonics on Modern and Ancient Active Plate Margins*, edited by J. K. Leggett, *Geol. Soc. Spec. Publ.*, *10*, 387–397.

McQuarrie, N. (2004), Crustal scale geometry of the Zagros fold-thrust belt, Iran, *J. Struct. Geol.*, *26*, 519–535.

McQuarrie, N., J. M. Stock, C. Verdel, and B. P. Wernicke (2003), Cenozoic evolution of Neotethys and implications for the causes of plate motions, *Geophys. Res. Lett.*, *30*(20), 2036, doi:10.1029/2003GL017992.

Meyer, B., F. Mouthereau, O. Lacombe, and P. Agard (2005), Evidence for Quaternary activity along the Deshir Fault: Implication for the Tertiary tectonics of central Iran, *Geophys. J. Int.*, *163*, 192–201, doi:10.1111/j.1365-246X.2005.02784.x.

Michard, A., B. Goffe, O. Saddiqi, R. Oberhänsli, and A. S. Wendt (1994), Late Cretaceous exhumation of the Oman blueschists and eclogites: A two-stage extensional mechanism, *Terra Nova*, *6*, 404–413.

Molinaro, M., P. Leturmy, J.-C. Guezou, D. Frizon de Lamotte, and S. A. Eshraghi (2005), The structure and kinematics of the southeastern Zagros fold-thrust belt, Iran: From thin-skinned to thick-skinned tectonics, *Tectonics*, *24*, TC3007, doi:10.1029/2004TC001633.

Montigny, R., O. Le Mer, R. Thuziat, and H. Whitechurch (1988), K-Ar and $^{40}Ar/^{39}Ar$ study of metamorphic rocks associated with the Oman ophiolite: Tectonic implications, *Tectonophysics*, *151*, 345–362.

Müller, R. D., W. R. Roest, J.-Y. Royer, L. M. Gahagan, and J. G. Sclater (1997), Digital isochrons of the world's ocean floor, *J. Geophys. Res.*, *102*, 3211–3214.

Okay, A. I. (1989), Alpine-Himalayan blueschists, *Annu. Rev. Earth Planet. Sci.*, *17*, 55–87.

Okay, A. I. (2002), Jadeite-chloritoid-glaucophane-lawsonite blueschists in north-west Turkey: Unusually high P/T ratios in continental crust, *J. Metamorph. Geol.*, *20*, 757–768.

Parra, T., O. Vidal, and P. Agard (2002), A thermodynamic model for Fe-Mg dioctahedral K white micas using data from phase-equilibrium experiments and natural pelitic assemblages, *Contrib. Mineral. Petrol.*, *143*, 706–732.

Paul, A., A. Kaviani, D. Hatzfeld, J. Vergne, and M. Mokhtari (2006), Seismological evidence for crustal-scale thrusting in the Zagros mountain belt (Iran), *Geophys. J. Int.*, *166*, 227–300.

Peacock, S. (1990), Numerical simulation of metamorphic pressure-temperature-time paths and fluid production in subduction slabs, *Tectonics*, *9*, 1197–1211.

Platt, J. P. (1986), Dynamics of orogenic wedges and the uplift of high-pressure metamorphic rocks, *Geol. Soc. Am. Bull.*, *97*, 1037–1053.

Platt, J. P. (1993), Exhumation of high-pressure rocks: A review of concepts and process, *Terra Nova*, *5*, 119–133.

Platt, J. P. (2000), Calibrating the bulk rheology of active obliquely convergent thrust belts and forearc wedges from surface profiles and velocity distributions, *Tectonics*, *19*, 529–548.

Platt, J. P., J. K. Leggett, J. Young, H. Raza, and S. Alam (1985), Large-scale sediment underplating in the Makran accretionary prism, southwest Pakistan, *Geology*, *13*, 507–511.

Poupeau, G., O. Saddiqi, A. Michard, B. Goffé, and R. Oberhänsli (1998), Late thermal evolution of the Oman mountains subophiolitic windows: Apatite fission-track thermochronology, *Geology*, *26*, 1139–1142.

Regard, V., C. Faccenna, J. Martinod, O. Bellier, and J. Thomas (2003), From subduction to collision: Control of deep processes on the evolution of convergent plate boundary, *J. Geophys. Res.*, *108*(B4), 2208, doi:10.1029/2002JB001943.

Regard, V., et al. (2005), Cumulative right-lateral fault slip rate across the Zagros-Makran transfer zone: Role of the Minab-Zendan fault system in accommodating Arabia-Eurasia convergence in southeast Iran, *Geophys. J. Int.*, *162*, 177–203.

Ricard, Y., and C. Vigny (1989), Mantle dynamics with induced plate tectonics, *J. Geophys. Res.*, *94*, 17,543–17,559.

Ricou, L. E. (1971), Le croissant ophiolitique péri-arabe, une ceinture de nappes mise en place au crétacé supérieur, *Rev. Geogr. Phys. Geol. Dyn.*, *13*, 327–350.

Ricou, L. E. (1994), Tethys reconstructed: Plates, continental fragments and their boundaries since 260 Ma from Central America to south-eastern Asia, *Geodin. Acta*, *7*, 169–218.

Ring, U., and M. T. Brandon (1999), Ductile deformation and mass loss in the Franciscan subduction complex: Implications for exhumation processes in accretionary wedges, in *Exhumation Processes: Normal Faulting, Ductile Flow and Erosion*, edited by U. Ring et al., *Geol. Soc. Spec. Publ.*, *154*, 55–86.

Robertson, A. H. F. (1987), Upper Cretaceous Muti Formation: Transition of a Mesozoic carbonate platform to a foreland basin in the Oman Mountains, *Sedimentology*, *34*, 1123–1142.

Sabzehei, M. (1974), Les mélanges ophiolitiques de la région d'Esfandageh (Iran méridional). Etude pétrologique et structurale; interprétation dans le cadre Iranien, Ph.D. thesis, 306 pp., Univ. Grenoble, Grenoble, France.

Sabzehei, M., M. Berberian, J. Roshanravan, H. Azizan, M. Nazemzadeh, N. Alavi-Tehrani, A. Houchmand-Zadeh, M. A. A. Nowgole-Sadat, and M. Madjidi (1994), Geological map of Hajiabad, scale 1/250,000, Geol. Surv. of Iran, Tehran.

Saddiqi, O., G. Poupeau, A. Michard, B. Goffé, and R. Oberhänsli (1995), Exhumation des roches métamorphiques HP-BT d'Oman: Datation par traces de fission sur zircons, *C. R. Acad.*, *320*, 1071–1077.

Samson, S. D., and E. C. Alexander (1987), Calibration of the interlaboratory $^{40}Ar/^{39}Ar$ dating standard, Mnhb-1, *Chem. Geol.*, *145*, 27–34.

Scaillet, S. (1996), Excess ^{40}Ar transport scale and mechanism in high-pressure phengites: A case study from an eclogitized metabasite of the Dora Maira nappe, western Alps, *Geochim. Cosmochim. Acta*, *60*, 1075–1090.

Schaeffer, O. A., H. W. Muller, and T. V. Grove (1977), Laser $^{39}Ar/^{40}Ar$ study of Apollo 17 basalts, *Geochim. Cosmochim. Acta*, *8*, 1489–1499.

Schmädicke, E., and T. M. Will (2003), Pressure-temperature evolution of blueschist facies rocks from Sifnos, Greece, and implications for the exhumation of high-pressure rocks in the central Aegean, *J. Metamorph. Geol.*, *21*, 799–811.

Schneider, J., D. Bosch, P. Monié, S. Guillot, A. Garcia-Casco, J. M. Lardeaux, R. L. Torres-Roldan, and G. Millan Trujillo (2004), Origin and evolution of the Escambray Massif (central Cuba): An example of HP/LT rocks exhumed during intraoceanic subduction, *J. Metamorph. Geol.*, *22*, 227–247.

Schröder, J. W. (1944), Essai sur la structure de l'Iran, *Eclogae Geol. Helv.*, *37*, 37–81.

Schwartz, S., J.-M. Lardeaux, S. Guillot, and P. Tricart (2000), Diversité du métamorphisme éclogitique dans le massif ophiolitique du Monviso (Alpes occidentales, Italie), *Geodin. Acta*, *13*, 169–188.

Searle, M. P., and J. Cox (1999), Tectonic setting, origin and obduction of the Oman ophiolite, *Geol. Soc. Am. Bull.*, *111*, 104–122.

Searle, M. P., D. J. Waters, H. N. Martin, and D. C. Rex (1994), Structure and metamorphism of blueschist-eclogite facies rocks from the north-eastern Oman Mountains, *J. Geol. Soc. London*, *151*, 555–576.

Searle, M. P., C. J. Warren, D. J. Waters, and R. R. Parrish (2004), Structural evolution, metamorphism and restoration of the Arabian continental margin, Saih Hatat region, Oman Mountains, *J. Struct. Geol.*, *26*, 451–473.

Sengör, A. M. C. (1990), A new model for the late Palaeozoic-Mesozoic tectonic evolution of Iran and implications for Oman, in *The Geology and Tectonics of the Oman Region*, edited by A. H. F. Robertson, M. P. Searle, and A. C. Ries, *Geol. Soc. Spec. Publ.*, *49*, 797–831.

Sengör, A. M. C., D. Altiner, A. Cin, T. Ustomer, and K. J. Hsu (1988), The origin and assembly of the Tethyside orogenic collage at the expense of Gondwana land, in *Gondwana and Tethys*, edited by M. G. Audley-Charles and A. Hallam, *Geol. Soc. Spec. Publ.*, *37*, 119–181.

Sepehr, M., and J. W. Cosgrove (2004), Structural framework of the Zagros Fold-Thrust Belt, Iran, *Mar. Pet. Geol.*, *21*, 829–843.

Shojaat, B., A. A. Hassanipak, K. Mobasher, and A. M. Ghazi (2003), Petrology, geochemistry and tectonics of the Sabzevar ophiolite, north central Iran, *J. Asian Earth Sci.*, *21*, 1053–1067.

Shreve, R. L., and M. Cloos (1986), Dynamics of sediment subduction, mélange formation and prism accretion, *J. Geophys. Res.*, *91*, 10,229–10,245.

Soffel, H., and H. Förster (1984), Polar wander path of the central-east-Iran microplate, including new results, *Neues Jahrb. Geol. Palaeontol. Abh.*, *168*, 165–172.

Spear, F. S. (1993), *Metamorphic Phase Equilibria and Pressure-Temperature-Time Paths*, 799 pp., Mineral. Soc. of Am., Washington, D. C.

Spear, F. S., and J. Selverstone (1983), Quantitative P-T paths from zoned minerals: Theory and tectonic implications, *Contrib. Mineral. Petrol.*, *83*, 348–357.

Stampfli, G. M., and G. D. Borel (2002), A plate tectonic model for the Paleozoic and Mesozoic constrained by dynamic plate boundaries and restored synthetic oceanic isochrons, *Earth Planet. Sci. Lett.*, *196*, 17–33.

Stöckhert, B., W. V. Maresch, M. Brix, C. Kaiser, A. Toetz, R. Kluge, and G. Kruckhansleuder (1995), Crustal history of Margarita Island (Venezuela) in detail: Constraint on the Caribbean plate-tectonic scenario, *Geology*, *23*, 787–790.

Stöcklin, J. (1968), Structural history and tectonics of Iran: A review, *Am. Assoc. Pet. Geol. Bull.*, *52*, 1229–1258.

Talebian, M., and J. Jackson (2002), Offset on the Main Recent Fault of NW Iran and implications for the late Cenozoic tectonics of the Arabia-Eurasia collision zone, *Geophys. J. Int.*, *150*, 422–439.

Vernant, P., et al. (2004), Contemporary crustal deformation and plate kinematics in Middle East constrained by GPS measurements in Iran and northern Oman, *Geophys. J. Int.*, *157*, 381–398.

Vidal, O., and T. Parra (2000), Exhumation paths of high-pressure metapelites obtained from local equilibria for chlorite-phengite assemblages, *Geol. J.*, *35*, 139–161.

Vidal, O., T. Parra, and F. Trotet (2001), A thermodynamic model for Fe-Mg aluminous chlorite using data from phase equilibrium experiments and natural pelitic assemblages in the 100° to 600°C, 1 to 25 kb range, *Am. J. Sci.*, *301*, 557–592.

Villa, I. M. (1998), Isotopic closure, *Terra Nova*, *10*, 42–47.

Von Blanckenburg, F., and J. H. Davies (1995), Slab breakoff: A model for syncollisional magmatism and tectonics in the Alps, *Tectonics*, *14*, 120–131.

Walker, R., and J. Jackson (2002), Offset and evolution of the Gowk fault, S.E. Iran: A major intra-continental strike-slip system, *J. Struct. Geol.*, *24*, 1677–1698.

Warren, C. J., R. R. Parrish, M. P. Searle, and D. J. Waters (2003), Dating the subduction of the Arabian continental margin beneath the Semail ophiolite, Oman, *Geology*, *31*, 889–892.

Warren, C. J., R. R. Parrish, D. J. Waters, and M. P. Searles (2005), Dating the geologic history of Oman's Semail ophiolite: Insights from U-Pb geochronology, *Contrib. Mineral. Petrol.*, *150*, 403–422.

Wei, C., and R. Powell (2006), Calculated phase relations in the system NCKFMASH (Na_2O-CaO-K_2O-FeO-MgO-Al_2O_3-SiO_2-H_2O) for high-pressure metapelites, *J. Petrol.*, *47*, 385–408.

Wei, C., R. Powell, and L. F. Zhang (2003), Eclogites from the south Tianshan, NW China: Petrological characteristic and calculated mineral equilibria in the Na_2O-CaO-FeO-MgO-Al_2O_3-SiO_2-H_2O system, *J. Metamorph. Geol.*, *21*, 163–179.

Willner, A. P., J. Glodny, T. V. Gerya, E. Godoy, and H.-J. Massonne (2004), A counterclockwise PTt path of high-pressure/low-temperature rocks from the Coastal Cordillera accretionary complex of south-central Chile: Constraints for the earliest stage of subduction mass flow, *Lithos*, *75*, 283–310.

Zeitler, P. K., et al. (2001), Crustal reworking at Nanga Parbat, Pakistan: Metamorphic consequences of thermal-mechanical coupling facilitated by erosion, *Tectonics*, *20*(5), 712–728.

P. Agard, W. Gerber, L. Jolivet, L. Labrousse, B. Meyer, B. Vrielynck, and P. Yamato, Laboratoire de Tectonique, UMR CNRS 7072, Université Paris 6, Case 129, Tour 46-0, 2E, 4 place Jussieu, F-75252 Paris Cedex 05, France. (philippe.agard@lgs.jussieu.fr)

M. Molinaro, Laboratoire de Tectonique, Université de Cergy Pontoise, 5, mail Gay-Lussac, Neuville-sur-Oise, F-95031 Cergy, France.

P. Monié, Laboratoire Dynamique de la Lithosphère, UMR CNRS 5573, Université Montpellier 2, Place E. Bataillon, F-34095, Montpellier Cedex 05, France.

J. Omrani, Geological Survey of Iran, Meraj Bd., Tehran, Iran.